

Front-end Weber-Fechner gain control enhances the fidelity of combinatorial odor coding

Nirag Kadakia¹ and Thierry Emonet^{1,2*}

*For correspondence:

thierry.emonet@yale.edu (TE)

¹Department of Molecular, Cellular, and Developmental Biology, Yale University, New Haven, CT 06511; ²Department of Physics, Yale University, New Haven, CT 06511

Abstract We showed previously (Gorur-Shandilya et al 2017) that *Drosophila* olfactory receptor neurons (ORNs) expressing the co-receptor Orco scale their gain inversely with mean odor intensity according to Weber-Fechner's law. Here we show that this front-end adaptation promotes the reconstruction of odor identity from dynamic odor signals, even in the presence of confounding background odors and rapid intensity fluctuations. These enhancements are further aided by known downstream transformations in the antennal lobe and mushroom body. Our results, which are applicable to various odor classification and reconstruction schemes, stem from the fact that this adaptation mechanism is not intrinsic to the identity of the receptor involved. Instead, a feedback mechanism adjusts receptor sensitivity based on the activity of the receptor-Orco complex, according to Weber-Fechner's law. Thus, a common scaling of the gain across Orco-expressing ORNs may be a key feature of ORN adaptation that helps preserve combinatorial odor codes in naturalistic landscapes.

Introduction

Animals identify and discriminate odors using olfactory receptors (Ors) expressed in olfactory receptor neurons (ORNs) (Joseph and Carlson, 2015; Buck and Axel, 1991; Clyne et al., 1999; Vosshall et al., 1999). Individual ORNs, which typically express a single Or, respond to many odorants, while individual odorants activate many distinct ORNs (Friedrich and Korschning, 1997; Hallem and Carlson, 2006; Wang et al., 2010; Nara et al., 2011). Odors are thus encoded by the combinatorial patterns of activity they elicit in the sensing periphery (Malnic et al., 1999; Wang et al., 2010; Hildebrand and Shepherd, 1997; Hallem and Carlson, 2006; de Bruyne et al., 2001; Friedrich and Korschning, 1997), patterns decoded downstream into behavioral response (Wilson, 2013; Davies et al., 2015). Still, ethologically-relevant odors are often mixed with background ones (Saha et al., 2013; Renou et al., 2015) and intensity can vary widely and rapidly as odors are carried by the wind (Murlis, 1992; Weissburg, 2000; Celani et al., 2014; Cardé and Willis, 2008). How are odors recognized reliably despite these confounds? In *Drosophila melanogaster*, ORN dose response curves exhibit similar Hill coefficients but distinct power-law distributed activation thresholds (Hallem and Carlson, 2006; Si et al., 2019), which together with inhibitory odorants enhance coding capacity (Si et al., 2019; Cao et al., 2017; Hallem and Carlson, 2006; Stevens, 2016). In antennal lobe (AL) glomeruli, mutual lateral inhibition normalizes population response, reducing the dependency of activity patterns on odor concentration (Asahina et al., 2009; Olsen et al., 2010). Further downstream, sparse connectivity to the mushroom body (MB) helps maintain neural representations of odors, and facilitates compressed sensing and associative learning schemes (Caron et al., 2013; Litwin-

41 **Kumar et al., 2017; Krishnamurthy et al., 2017; Dasgupta et al., 2017**). Finally, temporal features
 42 of neural responses contribute to concentration-invariant representations of odor identity (**Brown**
 43 **et al., 2005; Raman et al., 2010; Gupta and Stopfer, 2014; Wilson et al., 2017**).

44 Here we examine how short-time ORN adaptation at the very front-end of the insect olfactory
 45 circuit contributes to the fidelity of odor encoding. Our theoretical study is motivated by the recent
 46 discovery of invariances in the signal transduction and adaptation dynamics of ORNs expressing
 47 the co-receptor Orco. ORN response is initiated upon binding of odorant molecules to olfactory
 48 receptors (ORs), opening the ion channels they form with the co-receptor Orco (**Larsson et al., 2004;**
 49 **Butterwick et al., 2018**). Because of differences in odor-receptor affinities, the responses of ORNs
 50 to diverse odorants of the same concentration differ widely (**Hallez and Carlson, 2006; Montague**
 51 **et al., 2011; Stensmyr et al., 2012**). In contrast, downstream from this input nonlinearity, signal
 52 transduction and adaptation dynamics exhibit a surprising degree of invariance with respect to
 53 odor-receptor identity: reverse-correlation analysis of ORN response to fluctuating stimuli produces
 54 highly stereotyped, concentration-invariant response filters (**Martelli et al., 2013; Si et al., 2019;**
 55 **Gorur-Shandilya et al., 2017**).

56 These properties stem in part from an apparently invariant adaptive scaling law in ORNs:
 57 gain varies inversely with mean odor concentration according to the Weber-Fechner Law of psy-
 58 chophysics (**Weber, 1996; Fechner, 1860**), irrespective of the odor-receptor combination (**Gorur-**
 59 **Shandilya et al., 2017; Cafaro, 2016; Cao et al., 2016**). This invariance can be traced back to
 60 adaptative feedback mechanisms in odor transduction, upstream of ORN firing (**Nagel and Wilson,**
 61 **2011; Cao et al., 2016; Cafaro, 2016; Gorur-Shandilya et al., 2017**), which depend on the activity
 62 of the signaling pathway rather than on the identity of its receptor (**Nagel and Wilson, 2011**). The
 63 generality of the adaptive scaling suggests it could be mediated by the highly conserved Orco
 64 co-receptor (**Butterwick et al., 2018; Getahun et al., 2013, 2016; Guo et al., 2017**). Indeed, phospho-
 65 rylation sites have been recently identified on Orco, some being implicated in odor desensitization,
 66 albeit over much longer timescales (**Guo and Smith, 2017; Guo et al., 2017**).

67 While in a simpler system such as *E. coli* chemotaxis (**Waite et al., 2018**), adaptive feedback via the
 68 Weber-Fechner Law robustly maintains sensitivity over concentration changes, the implication for a
 69 multiple-channel system – which combines information from hundreds of cells with overlapping
 70 receptive fields – is less clear. Here we combine a biophysical model of ORN adaptive response and
 71 neural firing with various sparse signal decoding frameworks to explore how ORN adaptation with
 72 Weber-Fechner scaling affects combinatorial coding and decoding of odor signals spanning varying
 73 degrees of intensity, molecular complexity, and temporal structure. We find that this front-end
 74 adaptive mechanism promotes the accurate discrimination of odor signals from backgrounds
 75 of varying molecular complexity, and aids other known mechanisms of neural processing in the
 76 olfactory circuit to maintain representations of odor identity across environmental changes.

77 Results

78 Model of ORN sensing repertoire

79 To model ORN firing rates in response to time-dependent odor signals, we extended a minimal
 80 model (**Gorur-Shandilya et al., 2017**) that reproduces the Weber-Fechner gain adaptation and firing
 81 rate dynamics measured in individual *Drosophila* ORNs in response to Gaussian and naturalistic
 82 signals (code available on GitHub (**Kadakia, 2019**)).

83 We consider a repertoire of $M = 50$ ORN types that each express one type of Or together with
 84 the co-receptor Orco (**Larsson et al., 2004**). Within ORNs of type $a = 1, \dots, M$, Or-Orco complexes
 85 form non-selective cation channels (**Butterwick et al., 2018**) (**Figure 1A**) that switch between active
 86 and inactive conformations, while simultaneously binding to odorants i with affinity constants, K_{ai}^*
 87 and K_{ai} , respectively (**Nagel and Wilson, 2011; Gorur-Shandilya et al., 2017**). For simplicity we only
 88 consider agonists, i.e. $K_{ai}^* > K_{ai}$, and assume receptors can only bind one odorant at a time. The
 89 analysis can easily be extended to include inhibitory odorants, which increases coding capacity (**Cao**

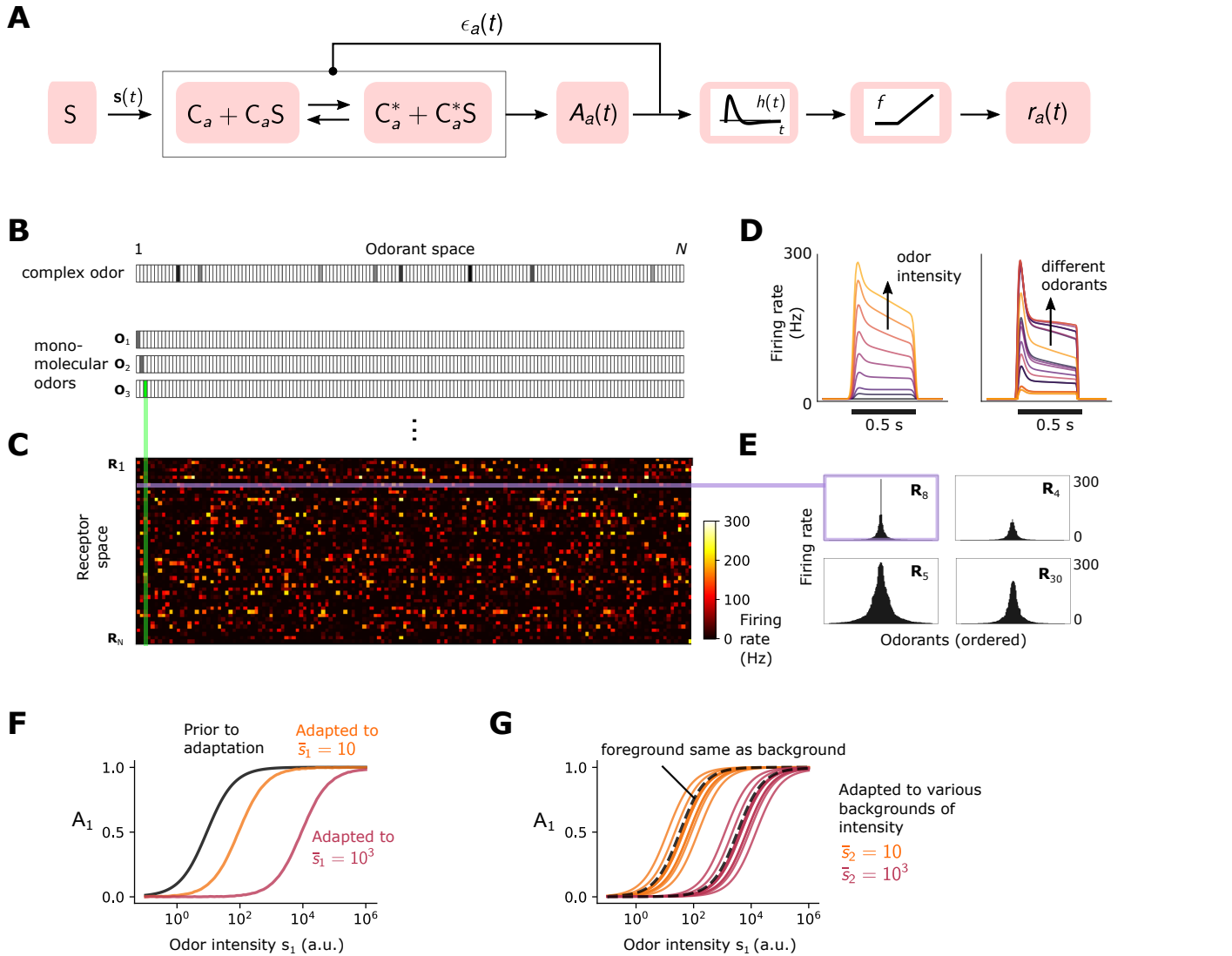


Figure 1. Simple ORN model. (Gorur-Shandilya et al., 2017) **A** Or/Orco complexes of type a switch between active C_a^* and inactive conformations C_a . Binding an excitatory odorant (S in the diagram) favors the active state. The active fraction is determined by the free energy difference between inactive and active conformations of the Or/Orco complex in its unbound state, $\epsilon_a(t)$ (in units of $k_B T$), and by odorant binding with affinity constants $K_a^* = (K_{a1}^*, \dots, K_{aN}^*)$ and K_a for the active and inactive conformations, respectively (Eqs. 1-2). Adaptation is mediated by a negative feedback (Nagel and Wilson, 2011) from the activity of the channel onto the free energy difference $\epsilon_a(t)$ with timescale τ . ORN firing rates $r_a(t)$ are generated by passing $A_a(t)$ through a linear temporal filter $h(t)$ and a nonlinear thresholding function f . **B** Odors are represented by N -dimensional vectors $s = [s_1, \dots, s_i, \dots, s_N]$, whose components s_i are the concentrations of the individual molecular constituents of s . **C** Step-stimulus firing rate of 50 ORNs to the $N=150$ possible monomolecular odors $s = s_i$, given power-law distributed affinity constants (Si et al., 2019). **D** Temporal responses of a representative ORNs to a pulse stimulus, for a single odorant at several intensities (left), or to many odors of the same intensity (right). **E** Representative ORN tuning curves (a single row of the response matrix in C, ordered by magnitude). Tuning curves are diverse, mimicking measured responses (Hallem and Carlson, 2006). **F** Dose-response of an ORN before (black) and after adaptation to either a low (yellow) or high (magenta) odor concentration. **G** Same, but the ORN was allowed to first adapt to one of various backgrounds of differing identities, before the foreground (same as in F) was presented. Also shown is the specific case when the foreground and background have the same identity (dashed lines).

90 *et al., 2017*). Dissociation (inverse affinity) constants are chosen from a power law distribution
 91 ($\alpha = 0.35$) recently found across ORN-odor pairs in *Drosophila* larvae (*Si et al., 2019*). For a handful of
 92 ORNs, we choose a very large value for one of the K_{ai}^* to mimic high responders to private odors
 93 relevant to innate responses (*Stensmyr et al., 2012*). These private odors do not affect the general
 94 findings.

95 Assuming that odorant binding and conformation changes are faster than other reactions in the
 96 signaling pathway, the fraction of channels of type a that are active at steady state is:

$$A_a(t) = \frac{C_a^* + C_a^* \mathbf{K}_a^* \cdot \mathbf{s}(t)}{C_a^* + C_a^* \mathbf{K}_a^* \cdot \mathbf{s}(t) + C_a + C_a \mathbf{K}_a \cdot \mathbf{s}(t)}. \quad (1)$$

97 C_a and C_a^* represent unbound channels in the inactive and active conformation. Here, $\mathbf{K}_a \cdot \mathbf{s}(t) =$
 98 $\sum_i^K K_{ai} s_i(t)$, where $s_i(t)$ is the time-dependent concentration of the i -th monomolecular component
 99 of the odor signal $\mathbf{s}(t)$ at time t (*Figure 1B*). $N = 150$ is the size of the molecular odorant space
 100 (*Figure 1B*). Eq. 1 can be rearranged as (derivation in Methods):

$$A_a(t) = \left[1 + \exp \left(\epsilon_a(t) + \ln \left(\frac{1 + \mathbf{K}_a \cdot \mathbf{s}(t)}{1 + \mathbf{K}_a^* \cdot \mathbf{s}(t)} \right) \right) \right]^{-1}. \quad (2)$$

101 The two terms in the exponential represent the change in the channel's free energy due to the
 102 binding of odorant i , and the free energy difference ϵ_a between the unbound states C_a and C_a^* , in
 103 units of $k_B T$. Because $K_{ai}^* > K_{ai}$, a sudden increase in the concentration of excitatory odor results in
 104 an increase in activity A_a .

105 Upon prolonged stimulation, ORNs adapt. At least one form of adaptation, which takes place
 106 over short time scale, $\tau \approx 250$ ms (*Gorur-Shandilya et al., 2017*), involves a negative feedback of
 107 the Or-Orco channel activity onto the channel sensitivity (*Nagel and Wilson, 2011; Gorur-Shandilya*
 108 *et al., 2017*). To model this adaptation process, we assume that inward currents elicited by activating
 109 Or-Orco channels eventually result in an increase of the free energy difference $\epsilon_a(t)$, possibly via a
 110 feedback onto Orco (*Butterwick et al., 2018*):

$$\tau \frac{d\epsilon_a(t)}{dt} = A_a(t) - A_{0a}, \quad (3)$$

111 where $\epsilon_{L,a} < \epsilon_a(t) < \epsilon_{H,a}$. The lower bound $\epsilon_{L,a}$ determines the spontaneous activity of the channel.
 112 The higher bound $\epsilon_{H,a}$ determines the concentrations of odors at which adaptation is unable to
 113 keep up and saturation occurs (*Gorur-Shandilya et al., 2017*). Through these dynamics, $\epsilon_a(t)$ can
 114 compensate for changes in free energy due to ligand binding (see Eq. 2), returning the activity
 115 A_a towards an adapted level A_{0a} above the spontaneous activity. Since ϵ_a is bounded below, a
 116 minimum amount of signal intensity is needed for adaptation to kick in. Finally, the firing rate is
 117 modeled by passing the activity $A_a(t)$ through the derivative-taking bi-lobed filter $h(t)$ and a rectifying
 118 nonlinearity f (*Gorur-Shandilya et al., 2017*):

$$r_a(t) = f(h(t) \otimes A_a(t)), \quad (4)$$

119 where \otimes is convolution. When deconvolved from stimulus dynamics, the shapes of the temporal
 120 kernels of *Drosophila* ORNs that express Orco tend to be stereotyped for many odor-receptor
 121 combination (*Martelli et al., 2013; Gorur-Shandilya et al., 2017; Si et al., 2019*) (although there
 122 are known exceptions such as super-sustained responses (*Montague et al., 2011*)). Moreover,
 123 adaptation is not intrinsic to the receptor (*Nagel and Wilson, 2011*). Accordingly, for simplicity τ ,
 124 $h(t)$, and f are assumed independent of receptor and odorant identities.

125 This minimal model reproduces the essential features of ORN response to odorant pulses (*Nagel*
 126 *and Wilson, 2011; Martelli et al., 2013; Cao et al., 2016*). In the absence of stimulus, ORNs fire

127 spontaneously at rates (1-10 Hz) (**Hallem and Carlson, 2006**) set by the lower free energy bound $\epsilon_{L,a}$,
 128 which we choose from a normal distribution (**Figure 1D**). For sufficiently strong stimuli, adaptation
 129 causes ϵ_a to increase, compensating for the drop in free energy difference due to ligand binding.
 130 This gradually reduces the firing rate to a steady state level $r(A_{0a}) \simeq 30\text{-}40$ Hz (**Gorur-Shandilya**
 131 *et al., 2017*) (**Figure 1D**). The diversity of temporal firing responses and tuning curves measured
 132 experimentally (**Hallem and Carlson, 2006; Montague et al., 2011; Brown et al., 2005; Gupta and**
 133 **Stopfer, 2014; Raman et al., 2010**) arise naturally in the model due to the distribution of chemical
 134 affinity constants and the nonlinearity of Eq. 2 (**Figure 1B-Figure 1E**).

135 The model also reproduces Weber-Fechner scaling of the gain with the inverse of the mean
 136 odorant intensity \bar{s}_i (**Gorur-Shandilya et al., 2017; Cao et al., 2016**). For small fluctuations Δs_i
 137 around \bar{s}_i , we have from Eq. 2 that $\Delta A_a / \Delta s_i \simeq A_a(\bar{s}_i) (1 - A_a(\bar{s}_i)) / \bar{s}_i$, whereby Weber's Law is
 138 satisfied provided $A_a(\bar{s}_i)$ is approximately constant (derivation in Methods). In our model, since
 139 the rate of adaptation depends only on the activity of the ion channel (right hand-side of Eq. 3),
 140 then in the adapted state we have $A_a(\bar{s}_i) \simeq A_{0a}$, ensuring that the gain scales like $1/\bar{s}_i$. This
 141 process adjusts the sensitivity of the ORN by matching the dose responses to the mean signal
 142 concentration, while maintaining their log-slopes (**Figure 1F**). However, for foreground odors mixed
 143 with background odors to which the system has adapted, the dose response curves now exhibit
 144 background-dependent shifts (**Figure 1G**).

145 While this phenomenological model could be extended to include further details – e.g. we
 146 could relax the quasi-steady-state assumption in Eq. 2, use a more complex model for channel
 147 adaptation and neural firing (**Gorur-Shandilya et al., 2017**), or consider feedforward mechanisms
 148 in addition to negative integral feedback (**Schulze et al., 2015**) – this minimally-parameterized form
 149 captures the key dynamical properties of Orco-expressing ORNs relevant to our study: receptor-
 150 independent adaptation (**Nagel and Wilson, 2011**) with Weber-Fechner scaling (**Gorur-Shandilya**
 151 *et al., 2017; Cafaro, 2016; Cao et al., 2016*) that maintains response time independent of mean
 152 stimulus intensity (**Martelli et al., 2013; Gorur-Shandilya et al., 2017**), along with a diversity of
 153 temporal firing patterns in response to a panel of monomolecular odorants (**Hallem and Carlson,**
 154 **2006; Montague et al., 2011; Brown et al., 2005; Gupta and Stopfer, 2014; Raman et al., 2010**)
 155 (**Figure 1D-1E**).

156 **Front-end Weber-Fechner adaptation preserves odor coding among background 157 and intensity confounds**

158 To investigate how front-end adaptation Weber-Fechner scaling affects the representations of
 159 odor identity within the repertoire of ORN response, we quantified the similarity between the
 160 responses \mathbf{r}_1 and \mathbf{r}_2 of the ORN repertoire to different stimuli s_1 and s_2 by measuring the Euclidean
 161 distance between \mathbf{r}_1 and \mathbf{r}_2 . Since it is not possible to visualize these 50-dimensional vectors, we
 162 projected them onto a lower-dimensional space using t-distributed stochastic neighbor embedding
 163 (t-SNE) (**van der Maaten and Hinton, 2008**). Like principle component analysis (PCA), t-SNE preserves
 164 similarity between objects (**Figure 2A**), but is more suitable than PCA for objects that are related
 165 nonlinearly – in our case, the dependency of firing rates on odor concentrations (Eq. 2).

166 We first examined how an adaptive or non-adaptive ORN repertoire encodes odor identity in an
 167 odor environment that contains a foreground odor s atop a background odor \bar{s} (**Figure 2B**). Both
 168 odors are sparse mixtures, with $K \ll N$ odorants of similar concentrations, odor “identity” being
 169 the particular set of odorants in the mixture. In the adaptive case, we assume that the system
 170 has fully adapted to the background \bar{s} before the foreground s is presented. This is enacted by
 171 calculating the firing response to the foreground odor $\mathbf{r}(s)$ only after having set the ϵ_a in Eq. 2 to
 172 their steady state values in response to the background odor \bar{s} :

$$\epsilon_a(\bar{s}) = \ln \left[\frac{1 - A_{0a}}{A_{0a}} \right] - (1 - \beta_a) \ln \left(\frac{1 + \mathbf{K}_a \cdot \bar{s}}{1 + \mathbf{K}_a^* \cdot \bar{s}} \right), \quad (5)$$

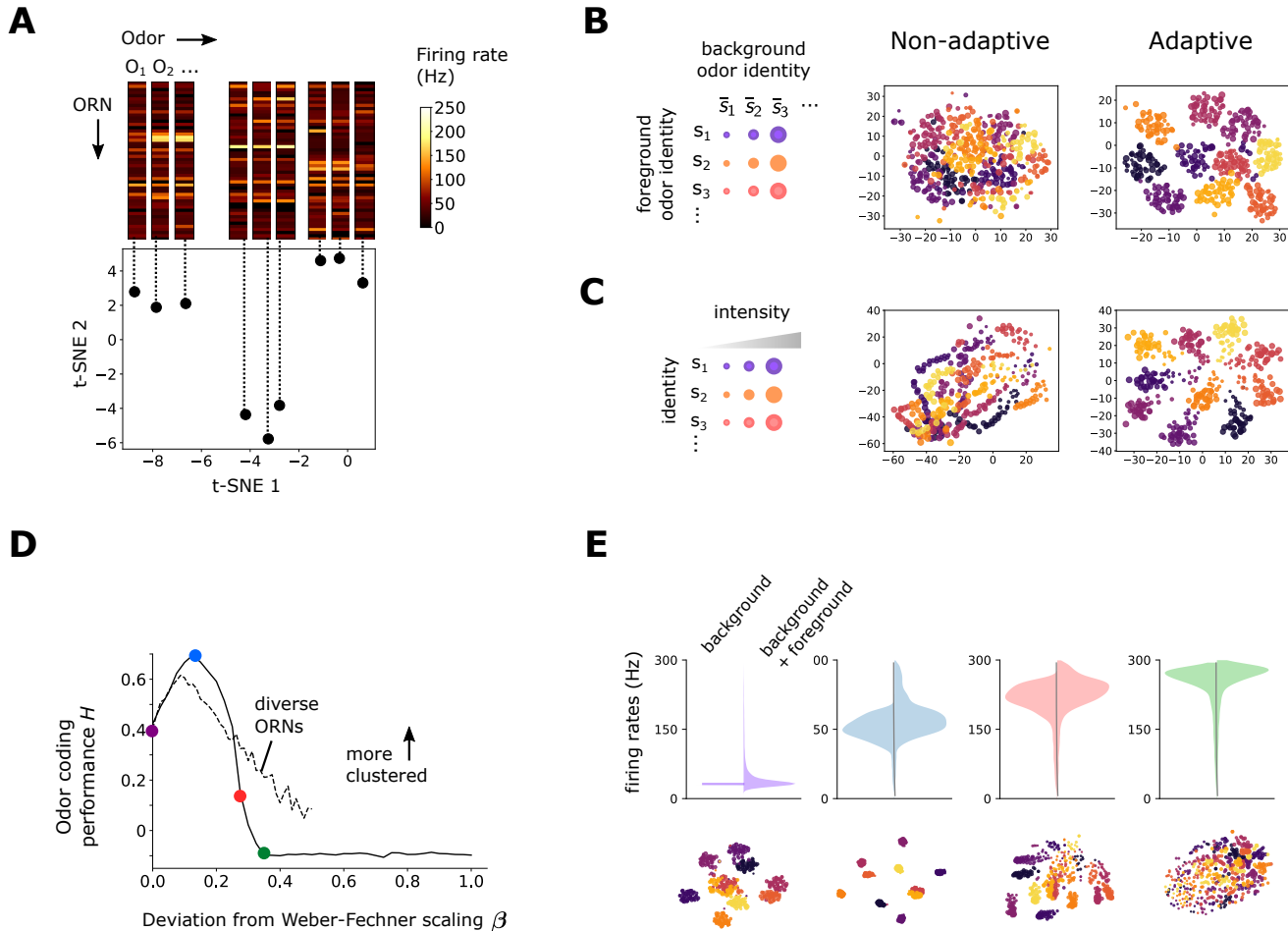


Figure 2. Front-end adaptation maintains representations of odor identity across background and intensity confounds. **A** Example t-SNE projection of the 50-dimensional vector of ORN firing rates to 2 dimensions. Each point represents the firing response to a distinct odor. Nearby points exhibit similarities in corresponding firing rates. **B** t-SNE projection of ORN firing rates, where each point represents the response to foreground odor s (point color) on top of a background odor \bar{s} (point size). In the adaptive system, e_a are set to their steady state values given the background odor \bar{s} alone according to Eq. 5 with $\beta = 0$. We assumed $A_{0a} = A_0$ for all a (we obtain similar results when A_{0a} are randomly distributed; **Figure 3–Figure Supplement 1**). Clustering by color implies that responses cluster by foreground odor identity. **C** Similar to (B), but now for odors whose concentrations span 4 decades (represented by point size). Here, the background odor identity is the same for all concentrations. **D** Performance of odor coding as a function of β , the magnitude of the deviation from Weber-Fechner's law ($\beta = 0$: Weber-Fechner's scaling; $\beta = 1$: no adaptation; see Eq. 5). Performance is quantified by the silhouette score H , which quantifies the degree by which responses cluster by foreground identity versus background identity in the t-SNE projections (1: highly clustered by foreground identity; 0 or slightly negative: not clustered) ((Rousseuw, 1987) and Methods). Line: same scaling $\beta_a = \beta$ for all ORNs. Dashed: β_a is uniformly distributed between 0 and $2\beta < 1$ (i.e. has mean β). **E** Distribution of ORN responses and t-SNE projections for $\beta = 0, 0.13, 0.28, 0.35$ in (D).

Figure 2–Figure supplement 1. t-SNE projections when background adapted activity level A_{0a} depends on ORN.

Figure 2–Figure supplement 2. Front-end adaptive feedback preserves information capacity of the ORN sensing repertoire.

173 where we have introduced the new parameter β_a to allow us to control the scaling of gain
 174 adaptation: for $\beta_a = 0$ the system exactly follows Weber-Fechner's law, while for $\beta_a = 1$ there is
 175 no adaptation. For small but nonzero β_a , the inverse gain scales sub-linearly (see Methods), and
 176 the adapted activity $A_a(\bar{s})$ increases weakly with background \bar{s} . In experiments, small deviations
 177 from the strict Weber-Fechner scaling on the order of $\beta \simeq 0.1$ are observed (see extended figures
 178 in ([Gorur-Shandilya et al., 2017](#))).

179 With Weber-Fechner's law in place for all ORNs ($\beta_a = 0$) responses cluster by the identity of
 180 foreground odor, showing that the repertoire of ORNs appropriately encodes the identity of novel
 181 odors irrespective of background signals – once these backgrounds have been “adapted away”
 182 ([Figure 2B](#)). This is the case regardless of whether A_{0a} is identical or different across neurons ([Figure
 183 2–Figure Supplement 1](#)). In contrast, when the system is non-adaptive, ($\beta_a = 1$), the responses
 184 exhibit weaker separations by odor identity ([Figure 2B](#)). Similarly, responses across different odor
 185 intensities are well separated by odor identity in the adaptive system, but less so in the non-adaptive
 186 system ([Figure 2C](#)). Calculating the mutual information between odor and ORN response in time
 187 shows that the adaptive system retains coding capacity as it confronts novel odors ([Figure 2–Figure
 188 Supplement 2](#)) whereas the non-adaptive system maintains coding capacity in a far more limited
 189 range of odor concentration.

190 To what extent do the benefits of front-end adaptation for odor coding depend on the precise
 191 Weber-Fechner scaling? We repeated the analysis from [Figure 2B](#) for increasing values of $\beta_a = \beta$
 192 between zero (Weber's law) (perfect adaptation) and one (no adaptation). To generalize [Figure 2B](#),
 193 we now let the intensities range over two decades. As β increases, the capacity of the system
 194 to cluster responses by odor identity degrades ([Figure 2D](#)). Introducing diversity among ORNs by
 195 distributing β_a 's uniformly between 0 and 2β (so that the mean is β) slightly increases performance
 196 at high β but reduces it at low β ([Figure 2D](#)). Overall, performance of odor coding degrades with β ,
 197 as poorly-adapting ORNs begin to saturate ([Figure 2D](#)).

198 Interestingly, besides this general trend, we find that for β very close to zero, a small deviation
 199 from Weber-Fechner's law instead *improves* odor coding. This arises because of the nonlinearity in
 200 the onset of adaptation: adaptation kicks in only when the strength of stimulus is sufficient for the
 201 response A_a to exceed A_{0a} , so that the right hand-side of Eq. 3 is positive. The minimum background
 202 intensity \bar{s} required for this to happen is given by $\epsilon_{L,a} = \epsilon_a(\bar{s})$, which, according to equation Eq. 5,
 203 increases with β . This initial effect increases odor coding performance, as the firing rates can
 204 distribute more broadly across the dynamical range of the ORNs, before adaptation is effected
 205 ([Figure 2E](#)). Thus, while Weber-Fechner scaling largely preserves the representation of foreground
 206 odor identity amid backgrounds, in some cases it may benefit from a slight relaxation so that the
 207 full dynamical range of the ORNs can be exploited.

208 **Front-end adaptation enhances odor decoding in complex environments**

209 How well does the preservation of odor coding translate to better signal reconstruction from ORNs
 210 responses? One potentially complicating factor is the disparity between sensor dimension and
 211 stimulus dimension: while *Drosophila* only express ~ 60 Or genes ([Vosshall et al., 2000](#)), the space
 212 of odorants is far greater ([Krishnamurthy et al., 2017](#)). An N -dimensional odor signal would naively
 213 need N sensory neurons to decode it – one for each odorant. However, naturally-occurring odors
 214 are sparse, typically comprised of only a few odorants. Enforcing sparsity of the signal during
 215 decoding greatly restricts the number of possible odors consistent with a given ORN response,
 216 suggesting that such high-dimensional signals might be inferred from less than N ORNs. Indeed, the
 217 decoding of sufficiently sparse signals from lower-dimensional responses is rigorously guaranteed
 218 by the theory of compressed sensing (CS) ([Donoho, 2006](#); [Candes et al., 2006a](#)). It is unknown
 219 whether CS is implemented in the *Drosophila* olfactory circuit ([Pehlevan et al., 2017](#)). Here we
 220 use this framework mainly as a tool to quantify how front-end adaptation potentially affects odor
 221 decoding, later verifying our conclusions with other classification techniques that incorporate the
 222 known architecture of the olfactory system.

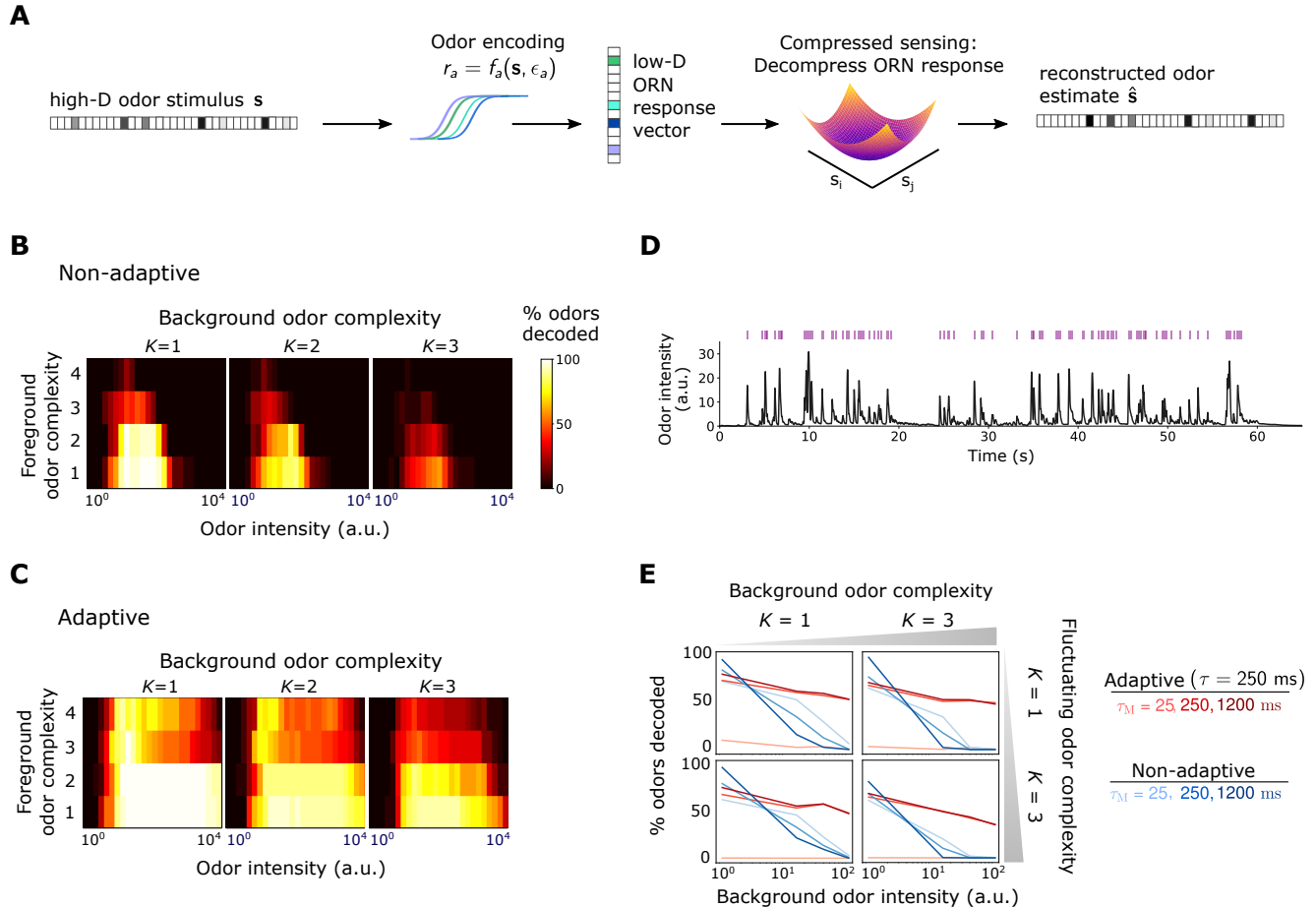


Figure 3. Front-end adaptation promotes accurate odor decoding in static and naturalistic odor environments. **A** Odor stimuli produce ORN responses via odor-binding and activation and firing machinery, as described by Eqs. 2-4. Odors are then decoded using compressed sensing optimization. Odors are assumed sparse, with K nonzero components, $K \ll N$. **B** Decoding accuracy of foreground odors in the presence of background odors, for a system without Weber Law adaptation. **C** Same as (B), with Weber Law adaptation. **D** Recorded trace of naturalistic odor signal; whiffs (signal > 4 a.u.) demarcated by purple bars. This signal is added to static backgrounds of different intensities and complexities. **E** Individual plots show the percent of accurately decoded odor whiffs as a function of background odor intensity, for the non-adaptive (blue) and adaptive (red) systems, for different τ_M (line shades).

Figure 3-Figure supplement 1. Decoding accuracy for system with ORN-dependent adaptive timescales τ .

Figure 3-Figure supplement 2. Decoding accuracy for system with ORN-dependent adapted firing rates.

Figure 3-Figure supplement 3. Decoding accuracy for receptors with multiple binding sites.

Figure 3-Figure supplement 4. Preservation of restricted isometry property in CS shows how decoding accuracy is maintained by adaptation.

Figure 3-Figure supplement 5. Odor decoding accuracy using the iterative hard thresholding algorithm for nonlinear compressed sensing.

Figure 3-Figure supplement 6. Whiff duration distribution in naturalistic stimulus.

223 In practice, CS is performed as a constrained linear optimization over the components of the
 224 signal vector – here, the odorant concentrations s_i . The constraints in the optimization are $\mathbf{r} = \mathbf{Ds}$,
 225 where \mathbf{D} is a matrix and \mathbf{r} are the measurements – here, \mathbf{r} would be the vector of ORN responses.
 226 The cost function to be minimized, $C = \sum_i |s_i|$, enforces sparsity by driving the estimate of each
 227 odorant component to zero; the constraints balance this tendency by simultaneously enforcing
 228 information from the ORN firing rates. The result is a reconstructed odor signal \hat{s} that is as sparse
 229 as possible, consistent with the ORN responses.

230 To incorporate the linear framework of CS into our nonlinear odor encoding model, we treat
 231 the nonlinear odor encoding exactly, but approximate the decoding to first order around the
 232 background concentration (*Figure 3A*). Specifically, we use Eqs. 2-4 to generate ORN responses \mathbf{r}
 233 for sparse odors \mathbf{s} having $K \ll N$ nonzero components $s_i = \bar{s}_i + \Delta s_i$, where the mean concentration
 234 is \bar{s}_i . To reconstruct these signals using CS, we minimize $\sum_i |\Delta s_i|$ while enforcing the constraints
 235 $\mathbf{r} = \mathbf{D}\Delta\mathbf{s}$, where \mathbf{D} is the linearization of Eq. 2 around \bar{s}_i (details in Methods). This linearization
 236 simplifies the CS decoding – namely it enforces a single, global minimum – but it is not critical for
 237 our general results; see Methods and *Figure 3–Figure Supplement 5*. The matrix \mathbf{D} depends on ϵ_a ,
 238 and as above, we assume precise adaptation by setting ϵ_a to their steady state values in response
 239 to the background odor alone (via Eq. 5 with $\beta = 0$). In the nonadaptive case, ϵ_a are held at their
 240 minimum values $\epsilon_{L,a}$.

241 We first examine how foreground odors are recognized when mixed with background odors of
 242 a distinct identity but similar intensities, quantifying decoding accuracy as the percentage of odors
 243 correctly decoded within some tolerance (see Methods). Without adaptation, accuracy is maintained
 244 within the range of receptor sensitivity for monomolecular backgrounds, but is virtually eliminated
 245 as background complexity rises (*Figure 3B*). The range of sensitivity is broader in the adaptive
 246 system, and is substantially more robust across odor concentration and complexity (*Figure 3C*).

247 In realistic odor environments, the concentration and duration of individual odor whiffs vary
 248 widely (*Celani et al., 2014*). We wondered how well a front-end adaptation mechanism with a
 249 single timescale τ could promote odor identity detection in such environments. As inputs to our
 250 coding/decoding framework, we apply a naturalistic stimulus intensity recorded using a photo-
 251 ionization detector (*Gorur-Shandilya et al., 2017*) (*Figure 3D*) to which we randomly assign sparse
 252 identities from the N -dimensional odorant space. To mimic background confounds, we combine
 253 these signals with static odor backgrounds, and then calculate the percentage of decoded whiffs.
 254 We assume the decoder has short-term memory: detected odor signals are only retained for
 255 τ_M seconds in the immediate past, bounding the amount of past information utilized in signal
 256 reconstruction.

257 Without ORN adaptation, sufficiently strong backgrounds eliminate the ability to reconstruct
 258 the identity of individual odor whiffs, irrespective of the complexity of either the foreground or
 259 background odor (*Figure 3E*, blue lines). In the adaptive system, this is substantially mitigated (red
 260 lines in *Figure 3E*), provided the memory duration τ_M is at least as long as the adaptation timescale
 261 τ (darker red lines). Because this short-term adaptation depends on the activity of the Or-Orco
 262 channel rather than on the identity of the receptor (*Nagel and Wilson, 2011; Martelli et al., 2013;*
 263 *Gorur-Shandilya et al., 2017*), the values of τ and A_{0a} were assumed the same for all ORNs; still,
 264 our results hold if these invariances are relaxed (*Figure 3–Figure Supplement 1* and *Figure 3–Figure*
 265 *Supplement 2*).

266 Front-end adaptation enhances primacy coding

267 The primacy coding hypothesis has recently emerged as an intriguing framework for combinatorial
 268 odor coding. Here, odor identity is encoded by the set (but not temporal order) of the p earliest
 269 responding glomeruli/ORN types, known as primacy set of order p (*Wilson et al., 2017*). If the
 270 activation order of ORNs were invariant to the strength of an odor step or pulse, primacy sets
 271 would in principle form concentration-invariant representation of odor identity. Though our coding
 272 framework uses the full ORN ensemble in signal reconstruction, some of these responses may

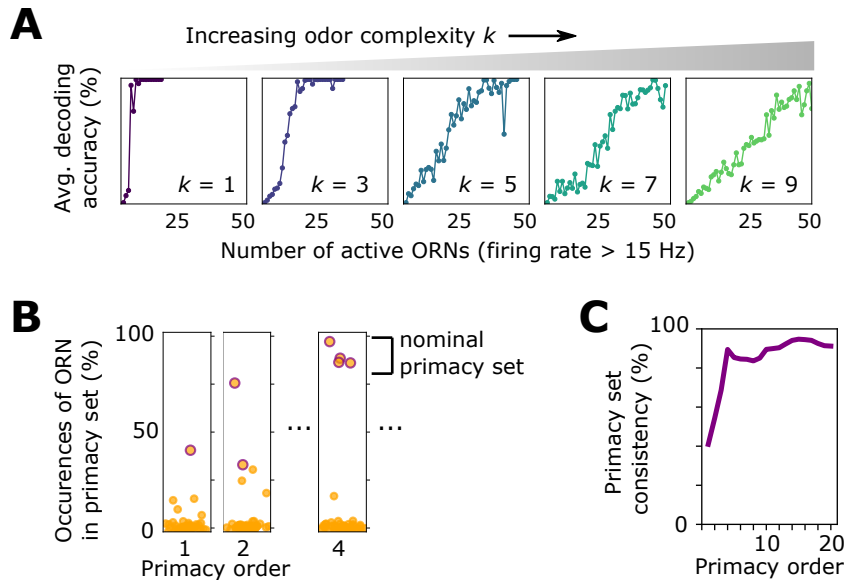


Figure 4. Effect of front-end adaptation on primacy coding. **A** Decoding accuracy as a function of the number of active ORNs, for different odor complexities. The primacy set consists of those ORNs required to be active for accurate decoding. **B** Frequency of particular ORNs in primacy sets of an odor placed atop different backgrounds. Individual plots show, for given primacy order p , the percentage of backgrounds for which the primacy set of odor A contains a given ORN (dots). Those with purple borders are the p most highly occurring – i.e. a nominal background-invariant primacy set for odor A. Points are jittered horizontally for visualization. **C** Consistency of primacy sets across backgrounds, as a function of p . Consistency is defined as the likelihood that an ORN in the nominal primacy set appears in any of the individual background-dependent primacy sets, averaged over the nominal set (average of the y -values of the purple dots in B). 100% consistency means that for all backgrounds, the primacy set of odor A is always the same p ORNs.

Figure 4–Figure supplement 1. Additional results for primacy coding in the adaptive ORN model.

273 contain redundant information, and a smaller primacy subset may suffice. To examine this, we
 274 apply our model to a sigmoidal stimulus that rises to half-max in 50 ms, calculating decoding
 275 accuracy in time. Since ORNs activate sequentially, the primacy set is defined by the ORN subset
 276 active when the odor is decoded. For simple odors, a limited set of earliest responding neurons
 277 fully accounts for the odor identity (**Figure 4A**), in agreement with primacy coding. As expected for
 278 more complex odor mixtures, the full repertoire is required for accurate decoding. Primacy coding
 279 also predicts that for stronger stimuli, responses occur earlier, since the primacy set is realized
 280 quicker, which our framework replicates (**Figure 4–Figure Supplement 1**).

281 Beyond mere consistency, however, front-end adaptation might also enhance primacy coding
 282 in different environments, such as background odors, which could scramble primacy sets. To
 283 investigate this, we considered again a sigmoidal odor step (odor A), now atop a static background
 284 (odor B) to which the system has adapted. We compared the primacy sets of odor A for 1000
 285 different choices of odor B, finding that primacy sets are highly consistent across background
 286 confounds for all but the smallest primacy orders (**Figure 4B–Figure 4C**). This also holds true for
 287 backgrounds of different concentrations (**Figure 4–Figure Supplement 1**), suggesting a central role
 288 for front-end adaptation in reinforcing primacy codes across differing environmental conditions.

289 Contribution of front-end adaptation for odor recognition within the *Drosophila* 290 olfactory circuit

291 Signal transformations in the sensing periphery are propagated through the remainder of the
 292 olfactory circuit. How does front-end adaptation interact with these subsequent neural transfor-
 293 mations? ORNs expressing the same OR converge to a unique AL glomerulus, where they receive
 294 lateral inhibition from other glomeruli (Olsen and Wilson, 2008; Asahina et al., 2009). This inhi-
 295 bition implements a type of divisive gain control (Olsen et al., 2010), normalizing the activity of

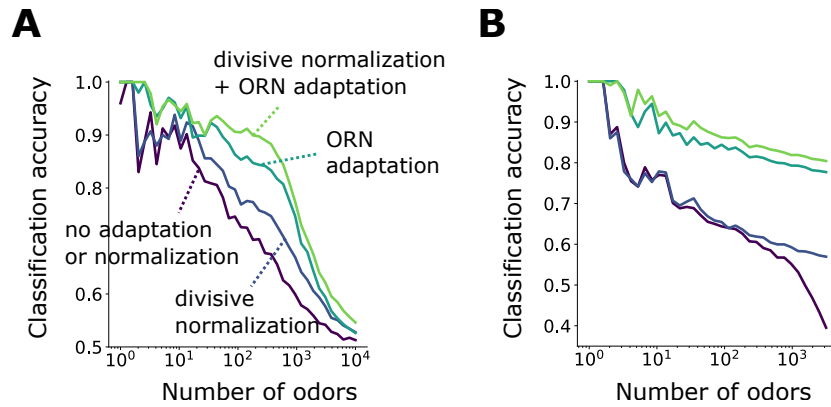


Figure 5. Front-end adaptation enhances odor recognition by the *Drosophila* olfactory circuit. **A** Accuracy of binary classification by odor valence, as a function of the number of distinct odor identities classified by the trained network (concentrations span 4 orders of magnitude), in systems with only ORN adaptation, only divisive normalization, both or neither. **B** Same as (A) but now classifying odors by identity.

Figure 5-Figure supplement 1. Binary classification for odors whose concentrations span a narrow range of concentration.

296 output projections neurons, which then synapse onto a large number of Kenyon cells (KCs) in the
 297 mushroom body. To investigate how odor representations are affected by interactions between
 298 front-end ORN adaptation and this lateral inhibition and synaptic divergence, we extended our ORN
 299 encoding model by adding uniglomerular connections from ORNs to the antennal lobe, followed by
 300 sparse, divergent connections to 2500 KCs (*Keene and Waddell, 2007; Litwin-Kumar et al., 2017;*
 301 *Caron et al., 2013*). Inhibition was modeled via divisive normalization, with parameters chosen
 302 according to experiment (*Olsen et al., 2010*). We quantified decoding accuracy by training and
 303 testing a binary classifier on the KC activity output of sparse odors of distinct intensity and identity,
 304 randomly categorized as appetitive or aversive. For simplicity, odor signals of the same identity
 305 but differing intensity were assigned the same valence. We trained the classifier on N_{ID} sparse
 306 odor identities at intensities chosen randomly over 4 orders of magnitude, then tested the classifier
 307 accuracy on the same odor identities but of differing concentrations.

308 Classification accuracy degrades to chance level as N_{ID} becomes very large (*Figure 5A*). When
 309 acting alone, either divisive normalization or ORN adaptation can help, although the effect of
 310 ORN adaptation is stronger. When both are active, accuracy improves further, suggesting that
 311 these distinct adaptive transformations may act jointly at different stages of neural processing in
 312 preserving representations of odor identity. As expected, these gains mostly vanish for the same
 313 odors chosen from a narrower range of concentrations (*Figure 5-Figure Supplement 1*).

314 If we train the classifier to distinguish odors by identity rather than valence, the benefits
 315 conferred by divisive normalization do not appear until N_{ID} is substantial, with accuracy below 65%
 316 for $N_{ID} > 50$ (*Figure 5B*). On the other hand, with ORN adaptation, accuracy remains above 85%
 317 for more than 1000 odor identities, strongly implicating front-end adaptation as a key player in
 318 maintaining odor identity representations, before signals are further processed downstream.

319 We note that previous simulation results have shown that divisive normalization aids identity
 320 decoding from PN response to a stronger degree than we find here (*Olsen et al., 2010*). The
 321 discrepancy may arise from the differences in odor classification from PN responses versus KC
 322 responses. It likely also arises from the fact that we are decoding odor mixtures rather than pure
 323 odorants, so the combinatorics may play a larger role. Finally, the divisive normalization model is
 324 a simple one in which glomeruli are all mutually inhibiting. A more complex model in which each
 325 glomerulus inhibits only a subset of other glomeruli through local neurons might produce a larger
 326 contribution.

327 Discussion

328 Weber-Law adaptation at the very front-end of the insect olfactory circuit (*Gorur-Shandilya et al., 2017; Cafaro, 2016; Cao et al., 2016*) may contribute significantly to the preservation of neural
 329 representations of odor identity amid confounding odors and intensity fluctuations. Drawing on
 330 experimental evidence for a number of ORN-invariant response features (*Nagel and Wilson, 2011; Martelli et al., 2013; Stevens, 2016; Gorur-Shandilya et al., 2017; Si et al., 2019*), we have found
 331 that this mechanism of dynamic adaptation confers significant benefits in coding fidelity, without
 332 the need for ORN-specific parameterizations. Still, our results hold when these invariances such as
 333 adaptation timescale or baseline activity are relaxed (*Figure 3-Figure Supplement 1 and Figure 3-Figure Supplement 2*). In the olfactory periphery, front-end Weber Law adaptation therefore
 334 appears fairly robust, a consequence of controlling gain via feedback from channel activity (*Waite et al., 2018; Nagel and Wilson, 2011; Gorur-Shandilya et al., 2017*), rather than through intrinsic,
 335 receptor-dependent mechanisms.

340 Our results also suggest that a slight breaking of Weber scaling may aid combinatorial coding,
 341 by spreading firing rates more fully over the ORN dynamic range, while still preventing saturation.
 342 The degree of this breaking would manifest as a correction to the Weber scaling exponent, \sim
 343 $(1/s)^1 \rightarrow \sim (1/s)^{1-\beta}$, which could in principle be measured experimentally for individual ORNs. Such
 344 small deviations from the strict Weber-Fechner scaling have been observed (see extended figures
 345 in (*Gorur-Shandilya et al., 2017*)).

346 While our framework incorporates many observed features of the *Drosophila* olfactory system –
 347 Weber-Law adaptation, power-law distributed receptor affinities, temporal filter invariance, connec-
 348 tivity topologies – it is minimal. We considered only one of the chemoreceptor families expressed
 349 in the fly antenna (*Joseph and Carlson, 2015*) and ignored possible contributions of odor bind-
 350 ing proteins (*Vogt and Riddiford, 1981; Menuz et al., 2014*), inhibitory odorants (*Cao et al., 2017*),
 351 and odorant-odorant antagonism (*Reddy et al., 2018*), which could further boost coding capacity
 352 and preserve representation sparsity. Useful extensions to our nonlinear-linear-nonlinear model
 353 might incorporate ephaptic coupling between ORNs housed in the same sensillum (*Su et al., 2012*),
 354 global inhibition in the mushroom body (*Papadopoulou et al., 2011*), and the effects of long-term
 355 adaptation (*Guo et al., 2017*).

356 Previous studies have characterized various neural mechanisms that help preserve combi-
 357 natorial codes. Lateral inhibition between glomeruli helps tame saturation and boost weak sig-
 358 nals (*Olsen et al., 2010*). The sparse degree of connectivity to either the olfactory bulb (vertebrates)
 359 or mushroom body (insects) may also be precisely tuned to optimize the capacity to learn associa-
 360 tions (*Litwin-Kumar et al., 2017*). In this work, we find that some of these downstream features act
 361 in concert with front-end dynamic adaptation in maintaining representations of odor identity.

362 Other studies have implicated the unique temporal patterns of neural response as signatures
 363 of odor identity (*Raman et al., 2010; Gupta and Stopfer, 2011; Brown et al., 2005; Gupta and*
364 Stopfer, 2014). ORN and projection neuron time traces form distinct trajectories in low-dimensional
 365 projections, and cluster by odor identity, much as we have found here for static responses at
 366 different concentrations (*Figure 2*). In locusts PNs, the trajectories elicited by foreground odors
 367 when presented in distinct backgrounds exhibit some degree of overlap; though partial, these
 368 overlaps were nonetheless sufficient to maintain background-invariant decoding from Kenyon
 369 cell responses (*Saha et al., 2013*). It was therefore suggested that background filtering likely
 370 occurs at the level of ORNs themselves (*Saha et al., 2013*). Likewise, in our framework, temporal
 371 coding is implicit: because the input nonlinearity depends on the diversity of binding affinities,
 372 odor signals are naturally formatted into temporal patterns that are both odor- and ORN-specific
 373 (*Figure 1D-Figure 1E*). Further, the short required memory timescales ($\tau_M \sim \tau \sim 250$ ms) suggest
 374 that only brief time windows are needed for accurate odor identification, consistent with previous
 375 findings (*Brown et al., 2005; Saha et al., 2013*). Moreover, we find that front-end adaptation
 376 enhances the robustness of other combinatorial coding schemes, such as primacy coding (*Wilson*

377 *et al., 2017*), which relies on the temporal order of ORN activation but not absolute firing rate
 378 (**Figure 4**).

379 In the well-characterized chemosensory system of bacterial chemotaxis, Weber Law adaptation
 380 is enacted through a feedback loop from the output activity of the receptor-kinase complexes onto
 381 the enzymes modifying receptor sensitivity (*Waite et al., 2018*). It is interesting that some aspects
 382 of this logic are also present in ORNs: although the molecular players are different (and still largely
 383 unknown, though likely involving calcium channel signaling (*Cao et al., 2016*)), it has been shown
 384 that transduction activity feeds back onto the sensitivity of Or-Orco ligand-gated cation channels,
 385 enabling the Weber-Fechner relation (*Nagel and Wilson, 2011; Gorur-Shandilya et al., 2017; Cao*
 386 *et al., 2016*). That this adaptation mechanism appears to act similarly across ORNs (*Gorur-Shandilya*
 387 *et al., 2017; Martelli et al., 2013; Cao et al., 2016*) suggests the possible involvement of the universal
 388 co-receptor Orco, whose role in long-term adaptation has recently been reported (*Getahun et al.,*
 389 *2013, 2016; Guo et al., 2017*). Further, the identification of 4 subunits comprising the Orco-Or ion
 390 channel suggest that generic Or/Orco complexes may contain multiple odorant binding sites, which
 391 when included in our model supports our general findings (**Figure 3-Figure Supplement 3**).

392 Weber Law ensures that sensory systems remain in the regime of maximum sensitivity, broad-
 393 ening dynamic range and maintaining information capacity (*Wark et al., 2007*). For a single-channel
 394 system, this requires matching the midpoint of the dose-response curve to the mean ligand con-
 395 centration (*Nemenman, 2012*), a strategy which may fail in multi-channel systems with overlapping
 396 tuning curves: adaptation to one signal could inhibit identification of others, if the signals excite
 397 some but not all of the same sensors, as in **Figure 1G**. Our results show that this strategy is still
 398 largely functional. In CS decoding, this can be traced to the observation that accuracy is guaranteed
 399 when sufficiently distinct odor identities produce sufficiently distinct ORN responses, a condition
 400 known as the restricted isometry property (*Candes et al., 2006a*). Indeed, the Weber-Fechner
 401 scaling increases the likelihood that this property is satisfied, beyond that in the non-adaptive
 402 system (SI text and **Figure 3-Figure Supplement 4-Figure 3-Figure Supplement 5**). Still, restricted
 403 isometry does not require that response repertoires are *invariant* to environmental changes. That
 404 is, even if the subset of active ORNs were concentration-dependent, odors could still in principle be
 405 fully reconstructible by CS. Nonetheless, our results in t-SNE clustering (**Figure 2**), primacy coding
 406 (**Figure 4B-4C**), and odor classification (**Figure 5**) suggest that some signature of response invariance
 407 emerges as a natural byproduct of front-end adaptation. Together, this implies that Weber Law
 408 adaptation, whether required by the olfactory circuit for precise signal reconstruction (as in CS)
 409 or for developing odor associations (as in classification), can play an integral part in maintaining
 410 combinatorial codes amid changing environmental conditions.

411 Methods and Materials

412 Adaptive ORN model

413 We model an odor as an N -dimensional vector $\mathbf{s} = [s_1, \dots, s_N]$, where $s_i > 0$ are the concentrations
 414 of individual volatile molecules (odorants) comprising the odor. The olfactory sensory system is
 415 modeled as a collection of M distinct Or/Orco complexes indexed by the sub index $a = 1, \dots, M$,
 416 each of which can be bound with any one of the odorant molecules, and can be either active
 417 (firing) or inactive (quiescent). At first we assume there is one binding site per complex; this will be
 418 generalized to many sites. We consider the binding and activation processes to be in equilibrium,
 419 assigning each state a corresponding Boltzmann weight, where the zero of energy is set by the
 420 unbound, inactive state C_a . These weights are:

$$\begin{aligned}
C_a &= 1 \\
C_a^* &= \exp(-\beta\epsilon_a) \\
C_a:s_i &= \exp(-\beta(-E_{ai} - \mu_i)) \\
C_a^*:s_i &= \exp(-\beta(-(E_{ai}^* - \epsilon_a) - \mu_i)),
\end{aligned} \tag{6}$$

421 where ϵ_a (assumed positive) is the free energy difference between the active and inactive con-
422 formation of the unbound receptor, and E_{ai} and E_{ai}^* are the free energy differences (assumed
423 positive) between the unbound and bound state for the inactive and active receptor, respec-
424 tively. $\mu_i = \mu_0 + \beta^{-1} \log(s_i/s_0)$ is the chemical potential for odorant species i in terms of a reference
425 chemical potential μ_0 at concentration s_0 , $s_0 \exp(-\beta\mu_0) = s_i \exp(-\beta\mu_i)$, which can be traded for the
426 thermodynamic-relevant disassociation constants $K_{ai}^{-1} = K_{D,ai} = s_0 e^{\beta(-E_{ai} - \mu_0)}$.

427 Adding up contributions from all i odorants, the active fraction is:

$$\begin{aligned}
A_a &= \frac{C_a^* + \sum_i C_a^*:s_i}{C_a^* + \sum_i C_a^*:s_i + C_a + \sum_i C_a:s_i} \\
&= \left(1 + \frac{C_a + \sum_i C_a:s_i}{C_a^* + \sum_i C_a^*:s_i} \right)^{-1} \\
&= \left(1 + e^{\epsilon_a} \frac{1 + \mathbf{K}_a \cdot \mathbf{s}(t)}{1 + \mathbf{K}_a^* \cdot \mathbf{s}(t)} \right)^{-1},
\end{aligned} \tag{2}$$

428 where we have expressed free energies in units of $k_B T = \beta^{-1}$ for notational convenience.

429 This expression can be generalized for the case of multiple, independent binding sites through
430 some simple combinatorial factors. Consider first an odorant i which can bind one of two locations
431 on receptor a . There are then 4 possible inactive states: both sites unbound, site 1 bound, site 2
432 bound, both sites bound. Combined with the active states, there are therefore 8 states for odorant
433 i and receptor a , with energies:

$$\begin{aligned}
\text{active} & \quad \{1, -E_{ai} - \mu_i, -E_{ai} - \mu_i, -2E_{ai} - 2\mu_i\} \\
\text{inactive} & \quad \{\epsilon_a, -(E_{ai}^* - \epsilon_a) - \mu_i, -(E_{ai}^* - \epsilon_a) - \mu_i, -(2E_{ai}^* - \epsilon_a) - 2\mu_i\}
\end{aligned} \tag{7}$$

434 In the active fraction, Eq. 2, the Boltzmann factors combine through the binomial theorem,
435 giving (for a single odorant environment i):

$$A_a(\text{odorant } i, 2 \text{ binding sites}) = \left[1 + e^{\epsilon_a} \left(\frac{1 + \mathbf{K}_a \cdot \mathbf{s}(t)}{1 + \mathbf{K}_a^* \cdot \mathbf{s}(t)} \right)^2 \right]^{-1}. \tag{8}$$

436 This expression generalizes for an arbitrary number of odorants and independent binding sites
437 through the appropriate combinatorial factors, giving an active fraction of

$$A_a(N \text{ odorants}, R \text{ binding sites}) = \left[1 + e^{\epsilon_a} \left(\frac{1 + \mathbf{K}_a \cdot \mathbf{s}(t)}{1 + \mathbf{K}_a^* \cdot \mathbf{s}(t)} \right)^R \right]^{-1}. \tag{9}$$

438 To generate ORN time traces, equations 2-3 are integrated numerically using the Euler method
439 with a 2 ms time step. For ORN firing (Eq. 4), $h(t)$ is bi-lobed (**Martelli et al., 2013**): $h(t) =$
440 $A p_{\text{Gam}}(t; \alpha_1, \tau_1) - B p_{\text{Gam}}(t; \alpha_2, \tau_2)$, $A = 190$, $B = 1.33$, $\alpha_1 = 2$, $\alpha_2 = 3$, $\tau_1 = 0.012$, and $\tau_2 = 0.016$, where
441 p_{Gam} is the pdf of $\text{Gamma}(\alpha, 1/\tau)$. Nonlinearity f is modeled as a linear rectifier with 5 Hz threshold.
442

443 **Derivation of ORN gain**

444 Weber's Law states that the gain, or differential response, of the receptor activity A_a scales with the
 445 mean odor concentration \bar{s}_i . To show how this is satisfied in our model, we consider the response,
 446 Eq. 2, to a signal $s = \bar{s} + \Delta s$, where Δs consists of only a small fluctuation in the i th component
 447 $\Delta s_i < |\bar{s}_i|$ about the mean. We derive the change in response to fluctuation Δs_i for general β from 0
 448 (Weber's law) to 1 (no adaptation).

449 First we write the activity in the form:

$$A_a = (1 + e^{F_a})^{-1}, \quad (10)$$

450 where

$$F_a = \epsilon_a(\bar{s}) + \ln \left(\frac{1 + \mathbf{K}_a \cdot \mathbf{s}}{1 + \mathbf{K}_a^* \cdot \mathbf{s}} \right), \quad (11)$$

451 where $\epsilon_a(\bar{s})$ is given by Eq. 5. Then, assuming $1/\mathbf{K}_a^* \ll s_i \ll 1/\mathbf{K}_a$, the change in response from
 452 the adapted level $A_a(\bar{s})$ is

$$\begin{aligned} A_a(s) - A_a(\bar{s}) = \Delta A_a &= \frac{dA_a}{dF_a} \frac{dF_a}{ds} \Big|_{\bar{s}} \Delta s_i \\ &= -\frac{e^{F_a}}{(1 + e^{F_a})^2} \Big|_{\bar{s}} \left(\frac{-K_{ai}^*}{\mathbf{K}_a^* \cdot \bar{s}} \right) \Delta s_i. \end{aligned} \quad (12)$$

453 We use Eq. 5 to evaluate e^{F_a} at \bar{s} , obtaining:

$$e^{F_a} \approx \frac{1 - A_{0a}}{A_{0a}} (\mathbf{K}_a^* \cdot \bar{s})^{-\beta}, \quad (13)$$

454 whereby

$$\begin{aligned} \frac{\Delta A_a}{\Delta s_i} &= \frac{\frac{1-A_{0a}}{A_{0a}} (\mathbf{K}_a^* \cdot \bar{s})^{-\beta}}{\left(1 + \frac{1-A_{0a}}{A_{0a}} (\mathbf{K}_a^* \cdot \bar{s})^{-\beta}\right)^2} \left(\frac{K_{ai}^*}{\mathbf{K}_a^* \cdot \bar{s}} \right) \\ &= \frac{(1 - A_{0a}) A_{0a} K_{ai}^*}{[A_{0a} (\mathbf{K}_a^* \cdot \bar{s})^{\frac{1+\beta}{2}} + (1 - A_{0a}) (\mathbf{K}_a^* \cdot \bar{s})^{\frac{1-\beta}{2}}]^2}. \end{aligned} \quad (14)$$

455 For $\beta = 0$ (the fully adaptive case) and a single odorant, this expression for the gain reduces to
 456 $(1 - A_{0a}) A_{0a} / s_i$. For small β , and given $A_{0a} \simeq 0.1$ (corresponding to 30 Hz on a 300 Hz firing rate scale),
 457 the denominator is dominated by the $1 - A_{0a}$ term, giving:

$$\frac{\Delta A_a}{\Delta s_i} \Big|_{(\beta \ll 1)} = \frac{A_{0a} K_{ai}^*}{(1 - A_{0a}) (\mathbf{K}_a^* \cdot \bar{s})^{1-\beta}}. \quad (15)$$

458 The implication of this is that the gain scaling of the inverse mean intensity, which is 1 for perfect
 459 adaptation (gain $\sim (1/s_i)^1$), is now sublinear. Thus, when Weber's Law is weakly broken, the gain still
 460 reduces with mean odor intensity, but not as quickly.

461

462 **t-SNE dimensionality reduction**

463 For t-SNE dimensionality reduction (*van der Maaten and Hinton, 2008*), ORN responses were
 464 generated for odor signal combinations consisting of 1 (among 10) distinct sparse foreground odors
 465 A atop 1 (among 50) distinct sparse background odors B, for **Figure 2B**. **Figure 2C** plots responses
 466 for 10 odors at 40 concentrations spanning 4 decades, atop a random sparse background odor of
 467 similar magnitude. For adaptive systems, ϵ_a were set to their fully adapted values to the background
 468 odor, given by Eq. 5, with $\beta = 0$. For **Figure 2D**, for each β , we averaged the silhouette score
 469 H (defined precisely below) over 5 different trials, each trial with a different seed for randomly
 470 choosing the odor identities.

471 To calculate performance of clustering in the t-SNE plots, we use the silhouette score H
 472 (*Rousseeuw, 1987*), which is a function of the 2D Euclidean distance $d(i, j|m, n)$ between the point p_{ij}
 473 representing odor s_i on background b_j and the point p_{mn} representing odor s_m on background b_n .
 474 For each p_{ij} , we define $a(ij)$ as:

$$475 \quad a(ij) = \frac{1}{1 - N_i} \sum_{n \in C_i} d(i, j|i, n) \quad (16)$$

475 where C_i is the set of all points in cluster i , i.e. with foreground i . This quantifies the average
 476 distance of p_{ij} to other points in the same cluster, i.e. with the same foreground but different
 477 backgrounds. We next define $b(ij)$ as:

$$478 \quad b(ij) = \min_{m \neq i} \frac{1}{N_m} \sum_{n \in C_m} d(i, j|m, n), \quad (17)$$

478 where the sum is taken over all points p_{mn} in cluster m – i.e. with foreground m not equal to i –
 479 and the minimum is taken over all clusters m . This quantifies the average distance from p_{ij} to the
 480 points in its "nearest neighbor" cluster. Then, H is defined as:

$$481 \quad H = \langle \frac{a(ij) - b(ij)}{\max\{a(ij), b(ij)\}} \rangle_{ij}, \quad (18)$$

481 where the average is taken over all points ij in the t-SNE plot. H is nearer to 1 when points clus-
 482 ter by foreground, and is near zero or slightly negative when the clusters cannot be disambiguated.
 483

484 **Compressed sensing decoding of ORN responses**

485 Compressed sensing (CS) addresses the problem of determining a sparse signal from a set of linear
 486 measurements, when the number of measurements is less than the signal dimension. Specifically,
 487 it is a solution to

$$488 \quad \mathbf{y} = \mathbf{D}\mathbf{x}, \quad (19)$$

488 where $\mathbf{x} \in \mathbb{R}^N$ and $\mathbf{y} \in \mathbb{R}^M$ are vectors of signals and responses, respectively, and \mathbf{D} is the
 489 measurement matrix. Since measurements are fewer than signal components, then $M < N$,
 490 whereby \mathbf{D} is wide rectangular and so Eq. 19 cannot be simply inverted to produce \mathbf{x} . The idea of CS
 491 is to utilize the knowledge that \mathbf{x} is sparse, i.e. only K of its components, $K \ll N$ are nonzero. Both
 492 the measurements and sparsity are thus combined into a single constrained optimization routine:

$$493 \quad \hat{\mathbf{x}}_i = \operatorname{argmin}_i \sum_i^K |\mathbf{x}_i| \quad \text{such that } \mathbf{y} = \mathbf{D}\mathbf{x} \quad (20)$$

493 where \hat{x}_i are the optimal estimates of the signal components and the sum, which is known as
 494 the L_1 norm of \mathbf{x} , is a natural metric of sparsity (**Donoho, 2006**).

495 The L_1 norm is a convex operation and the constraints are linear, so the optimization has a
 496 unique global minimum. To incorporate the nonlinear response of our encoding model into this
 497 linear framework, we assume that the responses are generated through the full nonlinear steady
 498 state response, Eq. 2- 4, but that the measurement matrix \mathbf{D} needed for decoding uses a linear
 499 approximation of this transformation. Expanding Eq. 4 around $\bar{s} = s - \Delta s$ gives

$$\begin{aligned}\Delta r_a(t) &= r_a(s(t)) - r_a(\bar{s}(t)) \\ \Delta r_a(t) &= \int^t d\tau h(t-\tau) \sum_i^N \frac{dA_{ai}}{ds_i} \Big|_{\bar{s}} \Delta s_i\end{aligned}\quad (21)$$

500 where

$$r_a(s_0) = \int^t d\tau h(t-\tau) \sum_i^N A_{0a} \quad (22)$$

501 and where $\frac{dA_{ai}}{ds_i} \Big|_{\bar{s}}$ is given by the right-hand side of Eq. 14 with $\beta = 0$. Eqs. 21 and 22 hold only
 502 for integrands above 5 Hz (and are zero below), as per the linear rectifier f . We assume that the
 503 neural decoder has access to background \bar{s} , presumed learned (this assumption can be relaxed;
 504 see below), and to the linearized response matrix, Eq. 14, but must infer the excess signals Δs_i
 505 from excess ORN firing rates $\Delta r_a(t)$. Thus, this corresponds to the CS framework (Eq. 20) via $\Delta \mathbf{r} \rightarrow \mathbf{y}$,
 506 $\Delta \mathbf{s} \rightarrow \mathbf{x}$, and $dA_{ai}/ds_i \Big|_{\bar{s}} \rightarrow \mathbf{D}$. We optimize the cost function in Eq. 20 using sequential least squares
 507 programming, implemented in Python through using the scientific package SciPy.

508 For our simulations, we let sparse components s_i be chosen as $s_i = \bar{s}_i + \Delta s_i$, where $\bar{s}_i = s_0$ and
 509 $\Delta s_i \sim \mathcal{N}(s_0/3, s_0/9)$. The measurement matrix \mathbf{D} depends on the free energy differences ϵ_a . For
 510 static stimuli, ϵ_a equals the fixed point of Eq. 3 in response to the background stimulus with $\beta = 0$.
 511 For fluctuating stimuli, ϵ_a is updated in time by continuously integrating $r_a(t)$, via Eqs. 3 and 4; thus,
 512 only knowledge of the response $r_a(t)$ are needed by the decoder. To quantify decoding accuracy,
 513 we treat the zero and nonzero components of the sparse odor vector separately. We demand that
 514 the K nonzero components \hat{s}_i of the estimated sparse vector are within 25% of their true values s_i ,
 515 and that the $N - K$ zero components are estimated less than 10% of s_0 . Together, this ensures that
 516 the odorants comprising the odor mixture are estimated sufficiently close to their concentrations,
 517 and that the remaining components are sufficiently small. Odor signals \mathbf{s} are considered correctly
 518 decoded if both of these conditions are satisfied for all components s_i . The relatively lax accuracy
 519 demanded on the nonzero components is to prevent oversensitivity on the unavoidable errors
 520 introduced by linearization. Qualitatively, our findings are robust to these choices.

521 The naturalistic odor signal (**Figure 3D**) was generated by randomly varying flow rates of ethyl
 522 acetate and measuring the concentration with a photo-ionization detector (**Gorur-Shandilya et al.,**
 523 **2017**). Statistics mirroring a turbulent flow (**Celani et al., 2014**) were verified (**Figure 3–Figure Sup-**
 524 **plement 6**).

525

526 **Iterative hard thresholding (IHT) and the restricted isometry property in compressed 527 sensing**

528 The purpose of response linearization (Eq. 21) is simply to apply compressed sensing reconstruction
 529 directly using linear programming, without worrying about issues of local minima in Eq. 20. This
 530 allows us to isolate the impact of Weber Law adaptation from the particularities of the numerics.
 531 An alternate technique for compressed signal reconstruction, *iterative hard thresholding* (IHT), does
 532 not minimize the constrained L_1 norm directly, rather applying a hard threshold to an iteratively

533 updated signal estimate (**Blumensath and Davies, 2009b**). IHT can be generalized straightforwardly
 534 to nonlinear constraints, and would actually dispense with the need for a learned background \bar{s} ,
 535 simply initializing the iterations from $\bar{s} = \mathbf{0}$. Remarkably, this technique works quite well even for non-
 536 linear measurements (**Blumensath, 2013**). We demonstrate the applicability of the IHT algorithm
 537 to our odor decoding system in **Figure 3–Figure Supplement 5**, which reproduces qualitatively the
 538 findings in the main text. For these calculations, no background odor was assumed, each iterative
 539 decoding being initialized $\bar{s} = \mathbf{0}$.

540 IHT provides an alternate computational technique of nonlinear CS, which could be used to both
 541 extend and verify our results. Further, it allows us to illustrate why Weber Law adaptation maintains
 542 signal reconstruction fidelity in our olfactory sensing model. Like CS using L_1 -norm minimization,
 543 IHT exhibits amenable reconstruction and convergence properties under the guarantee of the
 544 so-called restricted isometry property (RIP) (**Candes et al., 2006b**). Loosely, RIP measures how
 545 closely a matrix operator resembles an orthogonal transformation when acting on sparse vectors.
 546 The degree to which RIP is satisfied can be understood in terms of the spectrum of a measurement
 547 matrix \mathbf{D} . In particular, if λ_i are the eigenvalues of $\mathbf{D}_i^T \mathbf{D}_i$, where \mathbf{D}_i is any $k \times m$ submatrix of \mathbf{D} , and

$$1 - \delta_i \leq \lambda_{\min} \leq \lambda_{\max} \leq 1 + \delta_i \quad (23)$$

548 is satisfied for some δ_i , then \mathbf{D} satisfies the RIP with constant δ_i . Plainly, the RIP states that
 549 the eigenvalues of $\mathbf{D}_i^T \mathbf{D}_i$, when acting on k -sparse vectors, are centered around 1. Thus, to intuit
 550 why signal reconstruction breaks down in the non-adaptive sensing system, we can investigate the
 551 eigendecomposition of various linearizations of the measurement matrix. We do this now, starting
 552 with a brief description of the IHT.

In the linear setting, IHT seeks sparse signals via the following iterative procedure (**Blumensath and Davies, 2009b**):

$$\mathbf{s}_{i+1} = H_K(\mathbf{s}_i + \mu \mathbf{D}^T (\mathbf{s}_i + (\mathbf{y} - \mathbf{D}\mathbf{s}_i))) \quad (24)$$

553 where \mathbf{s}_i is the i th estimate of the sparse signal \mathbf{s} , μ is a step size for the iterations, and \mathbf{y}, \mathbf{D} are
 554 as defined above. $H_k(\cdot)$ is a thresholding function which sets all but the largest K values of its
 555 argument to zero. The nonlinear extension to IHT is (**Blumensath, 2013**):

$$\mathbf{s}_{i+1} = H_K(\mathbf{s}_i + \mu \mathbf{D}_{\mathbf{s}_i}^T (\mathbf{s}_i + (\mathbf{y} - \mathbf{D}(\mathbf{s}_i)))), \quad (25)$$

556 where \mathbf{D} is a nonlinear sensing function and $\mathbf{D}_{\mathbf{s}_i}$ is a linearization of \mathbf{D} about the point \mathbf{s}_i .
 557 Reconstructibility for k -sparse signals is guaranteed if $\mathbf{D}_{\mathbf{s}_i}$ satisfies RIP for all \mathbf{s}_i and all k -sparse
 558 vectors (**Blumensath and Davies, 2009b**). To get a sense of how this is preserved in the adaptive
 559 system, we calculate the eigenvalues for 1000 choices of \mathbf{s}_i , acting on random signals of given
 560 sparsity K (**Figure 3–Figure Supplement 4**). Since the RIP is sensitive to constant scalings of the
 561 measurement matrix (while the actual estimation problem is not), we scaled all columns of $\mathbf{D}_{\mathbf{s}_i}$ to
 562 norm unity (**Blumensath and Davies, 2009a**). This normalizes the eigenvalues of $\mathbf{D}_{\mathbf{s}_i}^T \mathbf{D}_{\mathbf{s}_i}$ to center
 563 near unity before calculating the eigendecomposition, allowing us to assess the degree to which the
 564 RIP is satisfied. This scaled matrix can be used directly in Eq. 25 (**Blumensath, 2013; Blumensath and Davies, 2009a**). The spectra of these matrices indicates that the RIP becomes far more weakly
 565 satisfied in the non-adaptive system than in the adaptive one, for sufficient odor complexity and
 566 intensity.
 568

569 Network model and classification

570 For the network model, the AL-to-MB connectivity matrix \mathbf{J}_1 , is chosen such that each KC connects
 571 pre-synaptically to 7 randomly chosen AL glomeruli (**Litwin-Kumar et al., 2017; Caron et al., 2013**).

572 The results shown in **Figure 5** are an average of 10 distinct instantiations of this random topology.
 573 The $Z = 2500$ KCs are then connected by a matrix \mathbf{J}_2 to a readout layer of dimension Q , where $Q = 2$
 574 for binary and $Q = N_{ID}$ for multi-class classification. Both AL-to-MB and MB-to-readout connections
 575 are perceptron-type with rectified-linear thresholds. The weights of \mathbf{J}_1 and \mathbf{J}_2 are chosen randomly
 576 from $\sim \mathcal{N}(0, 1/\sqrt{7})$ and $\sim \mathcal{N}(0, 1/\sqrt{Z})$, respectively. Only the \mathbf{J}_2 and the MB-to-output thresholds
 577 are updated during supervised network training, via logistic regression (for binary classification) or
 578 its higher-dimensional generalization, the softmax cross entropy (for multi-class classification).

579 Acknowledgements

580 NK was supported by a postdoctoral fellowship through the Swartz Foundation and by an NRSA
 581 postdoctoral fellowship through the NIH BRAIN Initiative under award number 1F32MH118700.
 582 TE was supported by NIH R01 GM106189. We thank Damon Clark, John Carlson, Mahmut Demir,
 583 Srinivas Gorur-Shandilya, Henry Mattingly, and Ann Hermunstad for comments on the manuscript.

584 References

- 585 Asahina, K., Louis, M., Piccinotti, S., and Vosshall, L. (2009). A circuit supporting concentration-invariant odor
 586 perception in *Drosophila*. *Journal of Biology*, 8(1):9.
- 587 Blumensath, T. (2013). Compressed sensing with nonlinear observations and related nonlinear optimization
 588 problems. *IEEE Transactions on Information Theory*, 69(6).
- 589 Blumensath, T. and Davies, M. E. (2009a). How to use the iterative hard thresholding algorithm. In *Proceedings of
 590 SPARS'09 - Signal Processing with Adaptive Sparse Structured Representations* (Saint Malo, France, April 2009).
- 591 Blumensath, T. and Davies, M. E. (2009b). Iterative hard thresholding for compressed sensing. *Applied and
 592 Computational Harmonic Analysis*, 27(3):265 – 274.
- 593 Brown, S. L., Joseph, J., and Stopfer, M. (2005). Encoding a temporally structured stimulus with a temporally
 594 structured neural representation. *Nature Neuroscience*, 8:1568–1576.
- 595 Buck, L. and Axel, R. (1991). A novel multigene family may encode odorant receptors: a molecular basis for odor
 596 recognition. *Cell*, 65(1):175–187.
- 597 Butterwick, J. A., del Mármlor, J., Kim, K. H., Kahlson, M. A., Rogow, J. A., walz, T., and Ruta, V. (2018). Cryo-em
 598 structure of the insect olfactory receptor orco. *Nature*, 560:447–452.
- 599 Cafaro, J. (2016). Multiple sites of adaptation lead to contrast encoding in the *Drosophila* olfactory system.
 600 *Physiological Reports*, 4(4):e12762.
- 601 Candes, E., Romberg, J., and Tao, T. (2006a). Stable signal recovery from incomplete and inaccurate measure-
 602 ments. *Communications on Pure and Applied Mathematics*, 59(8):1207–1223.
- 603 Candes, E., Romberg, J., and Tao, T. (2006b). Stable signal recovery from incomplete and inaccurate measure-
 604 ments. *Communications on Pure and Applied Mathematics*, LIX:1207–1223.
- 605 Cao, L.-H., Jing, B.-Y., Yang, D., Zeng, X., Shen, Y., Tu, Y., and Luo, D.-G. (2016). Distinct signaling of *Drosophila*
 606 chemoreceptors in olfactory sensory neurons. *Proceedings of the National Academy of Sciences*, 113(7):E902–
 607 E911.
- 608 Cao, L.-H., Yang, D., Wu, W., Zeng, X., Jing, B.-Y., Li, M.-T., Qin, S., Tang, C., Tu, Y., and Luo, D.-G. (2017). Odor-evoked
 609 inhibition of olfactory sensory neurons drives olfactory perception in *Drosophila*. *Nature Communications*,
 610 8(1):1357.
- 611 Cardé, R. T. and Willis, M. A. (2008). Navigational strategies used by insects to find distant, wind-borne sources
 612 of odor. *Journal of Chemical Ecology*, 34(7):854–866.
- 613 Caron, S., Ruta, V., Abbott, L., and Axel, R. (2013). Random convergence of olfactory inputs in the *Drosophila*
 614 mushroom body. *Nature*, 497(4774):113–117.
- 615 Celani, A., Villermaux, E., and Vergassola, M. (2014). Odor landscapes in turbulent environments. *Phys. Rev. X*,
 616 4:041015.

- 617 Clyne, P. J., Warr, C. G., Freeman, M. R., Lessing, D., Kim, J., and Carlson, J. R. (1999). A novel family of divergent
618 seven-transmembrane proteins: Candidate odorant receptors in drosophila. *Neuron*, 22(2):327 – 338.
- 619 Dasgupta, S., Stevens, C. F., and Navlakha, S. (2017). A neural algorithm for a fundamental computing problem.
620 *Science*, 358(6364):793–796.
- 621 Davies, A., Louis, M., and Webb, B. (2015). A model of drosophila larva chemotaxis. *PLOS Computational Biology*,
622 11(11):1–24.
- 623 de Bruyne, M., Foster, K., and Carlson, J. R. (2001). Odor coding in the drosophila antenna. *Neuron*, 30(2):537 –
624 552.
- 625 Donoho, D. (2006). Compressed sensing. *IEEE Transactions on Information Theory*, 52(4):1289–1306.
- 626 Fechner, G. T. (1860). *Elemente der psychophysik*. Breitkopf und Härtel.
- 627 Friedrich, R. W. and Korschning, S. I. (1997). Combinatorial and chemotopic odorant coding in the zebrafish
628 olfactory bulb visualized by optical imaging. *Neuron*, 18(5):737–752.
- 629 Getahun, M. N., Olsson, S. B., Lavista-Llanos, S., Hansson, B. S., and Wicher, D. (2013). Insect odorant response
630 sensitivity is tuned by metabotropically autoregulated olfactory receptors. *PLoS One*, 8(3):e58889.
- 631 Getahun, M. N., Thoma, M., Lavista-Llanos, S., Keesey, I., Fandino, R. A., Knaden, M., Wicher, D., Olsson, S. B., and
632 Hansson, B. S. (2016). Intracellular regulation of the insect chemoreceptor complex impacts odour localization
633 in flying insects. *Journal of Experimental Biology*, 219(21):3428–3438.
- 634 Gorur-Shandilya, S., Demir, M., Long, J., Clark, D. A., and Emonet, T. (2017). Olfactory receptor neurons use gain
635 control and complementary kinetics to encode intermittent odorant stimuli. *eLife*, 6:e27670.
- 636 Guo, H., Kunwar, K., and Smith, D. (2017). Odorant receptor sensitivity modulation in *Drosophila*. *The Journal of
637 Neuroscience*, 37(39):9465–9473.
- 638 Guo, H. and Smith, D. P. (2017). Odorant receptor desensitization in insects. *Journal of Experimental Neuroscience*,
639 11:1–5.
- 640 Gupta, N. and Stopfer, M. (2011). Insect olfactory coding and memory at multiple timescales. *Current Opinion in
641 Neurobiology*, 21:768–773.
- 642 Gupta, N. and Stopfer, M. (2014). A temporal channel for information in sparse sensory coding. *Neuron*, pages
643 2247–2256.
- 644 Hallem, E. and Carlson, J. (2006). Coding of odors by a receptor repertoire. *Cell*, 125(1):143–160.
- 645 Hildebrand, J. G. and Shepherd, G. M. (1997). Mechanisms of olfactory discrimination: converging evidence for
646 common principles across phyla. *Annual review of neuroscience*, 20(1):595–631.
- 647 Joseph, R. M. and Carlson, J. R. (2015). Drosophila chemoreceptors: A molecular interface between the chemical
648 world and the brain. *Trends in Genetics*, 31(12):683 – 695.
- 649 Kadakia, N. (2019). ORN-WL-gain-control. GitHub. <https://github.com/emonetlab/ORN-WL-gain-control.git>.
650 926cfa7.
- 651 Keene, A. C. and Waddell, S. (2007). *Drosophila* olfactory memory: single genes to complex neural circuits. *Nature
652 Reviews Neuroscience*, 8:341–354.
- 653 Krishnamurthy, K., Hermundstad, A. M., Mora, T., Walczak, A. M., and Balasubramanian, V. (2017). Disorder and
654 the neural representation of complex odors: smelling in the real world. *bioRxiv*, doi:10.1101/160382.
- 655 Larsson, M. C., Domingos, A. I., Jones, W. D., Chiappe, M., Amrein, H., and Vosshall, L. B. (2004). Or83b encodes a
656 broadly expressed odorant receptor essential for drosophila olfaction. *Neuron*, 43(5):703 – 714.
- 657 Litwin-Kumar, A., Harris, K. D., Axel, R., Sompolsky, H., and Abbott, L. (2017). Optimal degrees of synaptic
658 connectivity. *Neuron*, 93(5):1153 – 1164.e7.
- 659 Malnic, B., Hirono, J., Sato, T., and Buck, L. B. (1999). Combinatorial receptor codes for odors. *Cell*, 96(5):713–723.
- 660 Martelli, C., Carlson, J. R., and Emonet, T. (2013). Intensity invariant dynamics and odor-specific latencies in
661 olfactory receptor neuron response. *Journal of Neuroscience*, 33(15):6285–6297.

- 662 Menuz, K., Larter, N. K., Park, J., and Carlson, J. R. (2014). An rna-seq screen of the drosophila antenna identifies
663 a transporter necessary for ammonia detection. *PLoS Genetics*, 10(11):e1004810.
- 664 Montague, S. A., Mathew, D., and Carlson, J. R. (2011). Similar odorants elicit different behavioral and physiological
665 responses, some supersustained. *Journal of Neuroscience*, 31(21):7891–7899.
- 666 Murlis, J. (1992). Odor plumes and how insects use them. *Annual Review of Entomology*, 37:505–532.
- 667 Nagel, K. and Wilson, R. (2011). Biophysical mechanisms underlying olfactory receptor neuron dynamics. *Nature
668 Neuroscience*, 14:208–216.
- 669 Nara, K., Saraiva, L. R., Ye, X., and Buck, L. B. (2011). A large-scale analysis of odor coding in the olfactory
670 epithelium. *Journal of Neuroscience*, 31(25):9179–9191.
- 671 Nemenman, I. (2012). Information theory and adaptation. In Wall, M. E., editor, *Quantitative Biology: From
672 Molecular to Cellular Systems*, chapter 4, pages 73–91. CRC Press, USA.
- 673 Olsen, S. R., Vikas, B., and Wilson, R. I. (2010). Divisive normalization in olfactory population codes. *Neuron*,
674 66:287–299.
- 675 Olsen, S. R. and Wilson, R. I. (2008). Lateral presynaptic inhibition mediates gain control in an olfactory circuit.
676 *Nature*, 452:952–960.
- 677 Papadopoulou, M., Cassenaer, S., Nowotny, T., and Laurent, G. (2011). Normalization for sparse encoding of
678 odors by a wide-field interneuron. *Science*, 332(6030):721–725.
- 679 Pehlevan, C., Genkin, A., and Chklovskii, D. B. (2017). A clustering neural network model of insect olfaction. In
680 *2017 51st Asilomar Conference on Signals, Systems, and Computers*, pages 593–600.
- 681 Raman, B., Joseph, J., Tang, J., and Stopfer, M. (2010). Temporally diverse firing patterns in olfactory receptor
682 neurons underlie spatiotemporal neural codes for odors. *Journal of Neuroscience*, 30(6):1994–2006.
- 683 Reddy, G., Zak, J., Vergassola, M., and Murthy, V. N. (2018). Antagonism in olfactory receptor neurons and its
684 implications for the perception of odor mixtures. *eLife*, 7:344958.
- 685 Renou, M., Party, V., Rouyar, A., and Anton, S. (2015). Olfactory signal coding in an odor background. *Biosystems*,
686 136:35 – 45.
- 687 Rousseeuw, P. J. (1987). Silhouettes: A graphical aid to the interpretation and validation of cluster analysis.
688 *Journal of Computational and Applied Mathematics*, 20:53–65.
- 689 Saha, D., Leong, K., Peterson, S., Siegel, G., and Raman, B. (2013). A spatiotemporal coding mechanism for
690 background-invariant odor recognition. *Nature Neuroscience*, 16:1830–1839.
- 691 Schulze, A., Gomez-Marin, A., Rajendran, V. G., Lott, G., Musy, M., Ahammad, P., Deogade, A., Sharpe, J., Riedl, J.,
692 Jarriault, D., Trautman, E. T., Werner, C., Venkadesan, M., Druckmann, S., Jayaraman, V., and Louis, M. (2015).
693 Dynamical feature extraction at the sensory periphery guides chemotaxis. *eLife*, 4:e06694.
- 694 Si, G., Kanwal, J., Hu, Y., Tabone, C. J., Baron, J., Berck, M. E., Vignoud, G., and Samuel, A. D. (2019). Invariances in
695 a combinatorial olfactory receptor code. *Neuron*, 101:950–962.
- 696 Stensmyr, M. C., Dweck, H. K., Farhan, A., Ibba, I., Strutz, A., Mukunda, L., Linz, J., Grabe, V., Steck, K., Lavista-
697 Llanos, S., Wicher, D., Sachse, S., Knaden, M., Becher, P. G., Seki, Y., and Hansson, B. S. (2012). A conserved
698 dedicated olfactory circuit for detecting harmful microbes in drosophila. *Cell*, 151(6):1345 – 1357.
- 699 Stevens, C. F. (2016). A statistical property of fly odor responses is conserved across odors. *Proceedings of the
700 National Academy of Sciences*, 113(24).
- 701 Su, C.-Y., Menuz, K., Reisert, J., and Carlson, J. (2012). Non-synaptic inhibition between grouped neurons in an
702 olfactory circuit. *Nature*, 492(7427):76–71.
- 703 van der Maaten, L. and Hinton, G. (2008). Visualizing high-dimensional data using t-sne. *Journal of Machine
704 Learning Research*, 9:2579–2605.
- 705 Vogt, R. G. and Riddiford, L. M. (1981). Pheromone binding and inactivation by moth antennae. *Nature*,
706 293(5828):161.

- 707 Vosshall, L. B., Amrein, H., Morozov, P. S., Rzhetsky, A., and Axel, R. (1999). A spatial map of olfactory receptor
708 expression in the drosophila antenna. *Cell*, 96(5):725 – 736.
- 709 Vosshall, L. B., Wong, A. M., and Axel, R. (2000). An olfactory sensory map in the fly brain. *Cell*, 102(2):147 – 159.
- 710 Waite, A. J., Frankel, N. W., and Emonet, T. (2018). Behavioral variability and phenotypic diversity in bacterial
711 chemotaxis. *Annual Review of Biophysics*, 47(1):595–616. PMID: 29618219.
- 712 Wang, G., Carey, A. F., Carlson, J. R., and Zwiebel, L. J. (2010). Molecular basis of odor coding in the malaria vector
713 mosquito anopheles gambiae. *Proceedings of the National Academy of Sciences*, 107(9):4418–4423.
- 714 Wark, B., Lundstrom, B. N., and Fairhall, A. (2007). Sensory adaptation. *Current Opinion in Neurobiology*,
715 17(4):423–429.
- 716 Weber, E. H. (1996). *EH Weber on the tactile senses*. Psychology Press.
- 717 Weissburg, M. (2000). The fluid dynamical context of chemosensory behavior. *The Biological Bulletin*, 198(2):188–
718 202. PMID: 10786940.
- 719 Wilson, C. D., Serrano, G. O., Koulakov, A. A., and Rinberg, D. (2017). A primacy code for odor identity. *Nature
720 Communications*, 8(1):1477.
- 721 Wilson, R. I. (2013). Early olfactory processing in *Drosophila*: mechanisms and principles. *Annual Review of Neuroscience*,
722 36(1):217–241.

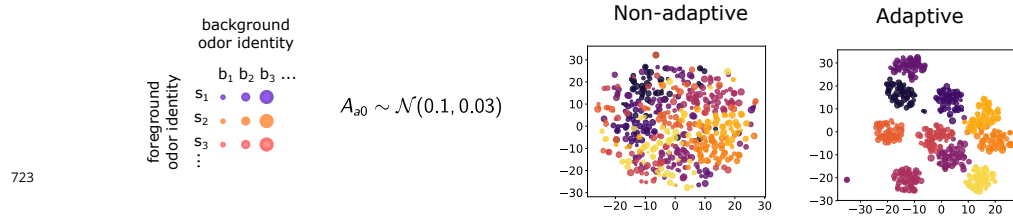


Figure 2-Figure supplement 1. t-SNE projections for non-adaptive ($\beta = 1$) and adaptive ($\beta = 0$) systems, when background firing rates depend on ORN identity. Background active fractions A_{0a} are chosen normally with mean 0.1 and deviation 0.03, corresponding to background firing rates around of $\simeq 20\text{-}40$ Hz.

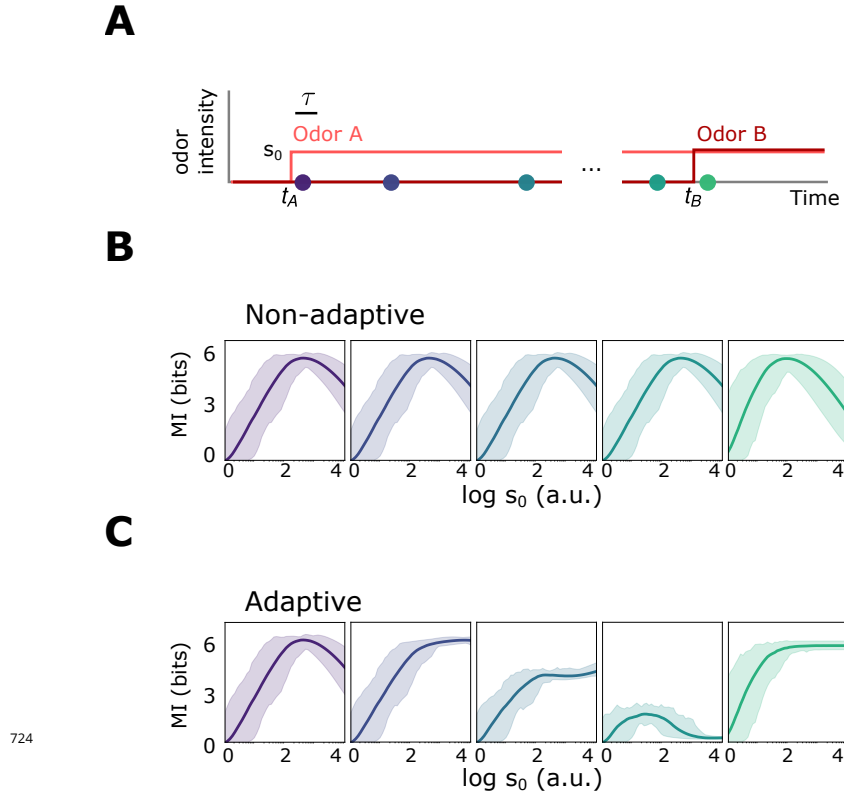


Figure 2–Figure supplement 2. Front-end adaptive feedback preserves information capacity of the ORN sensing repertoire. **A** Mutual information between signal $s(t) = s_A(t) + s_B(t)$ and response $r(t)$ is calculated at various points in time t for an odor environment consisting of two step odors, A and B. Odor A, with concentration $s_A(t)$, turns on at time t_A and odor B, with concentration $s_B(t)$, turns on at some later time t_B . Both odors have similar intensities $\sim s_0$ and similar molecular complexity ($k = 4$). **B** Mutual information as a function of s_0 for the non-adaptive system, respectively, at different time points after t_A , corresponding to the dots in A. The mutual information carried by distinct ORNs is represented by the shaded region; their average is plotted by the heavy line. In the non-adaptive system, the mutual information peaks in the regime of high sensitivity after the arrival of odor A (purple, blue), and shifts leftward with the onset of odor B (teal, green). The leftward shifts occurs since stronger signals are more prone to response saturation (compromising information transfer) as odor B arrives. **C** Same as B, now for the adaptive system. The MI mimics the non-adaptive case at the onset of odor A, before adaptation has kicked in (purple). As the system adapts and responses decrease toward baseline, previously saturating signal intensities now cross the regime of maximal sensitivity, which therefore shifts rightward to higher s_0 (dark blue). Much later, but before the arrival of odor B, the ORNs that responded now fire at a similar adapted firing rate ~ 30 Hz, irrespective of odor identity, so the mutual information drops to zero. However, having now adjusted its sensitivity to the presence of odor A, the system can respond appropriately to odor B: the MI at t_B is nearly 6 bits across decades of concentration immediately following t_B (green).

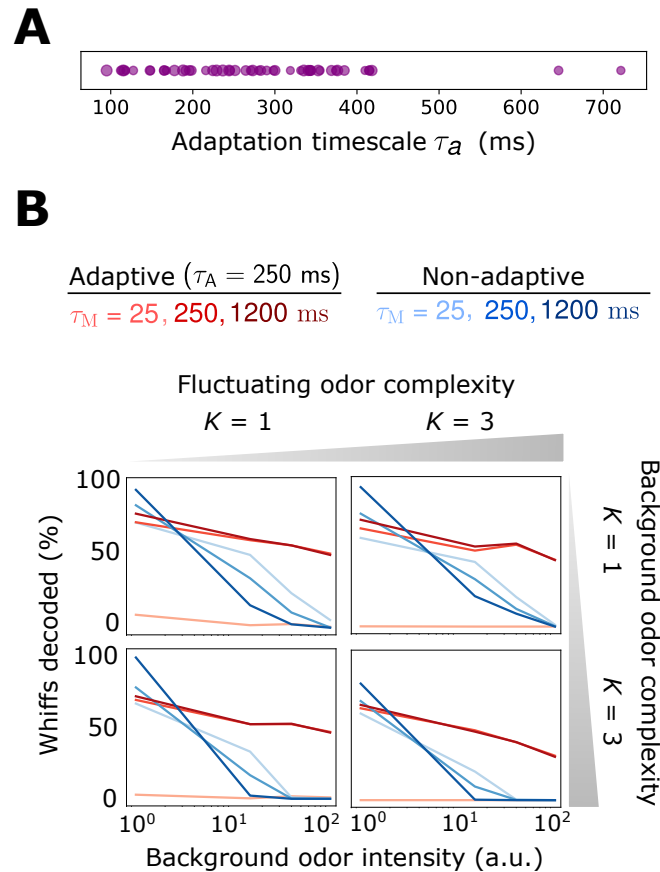


Figure 3-Figure supplement 1. Decoding accuracy for system with ORN-dependent adaptive timescales τ_a . **A** Distribution of timescales for all ORNs a (purple dots). Here, $\tau_a \sim \tau 10^X$ where $\tau = 250$ ms as in the main text and $X \sim \mathcal{N}(0, 0.2)$. **B** Individual plots show the percent of accurately decoded odor whiffs (same fluctuating odor signal used in the main text) as a function of background odor intensity, for the non-adaptive (blue) and adaptive (red) systems, for different τ_M (line shades). Plots are arrayed by the complexity of the naturalistic signal (column-wise) and the complexity of the background odor (row-wise).

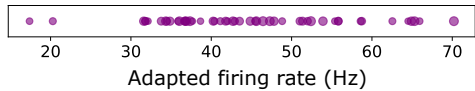
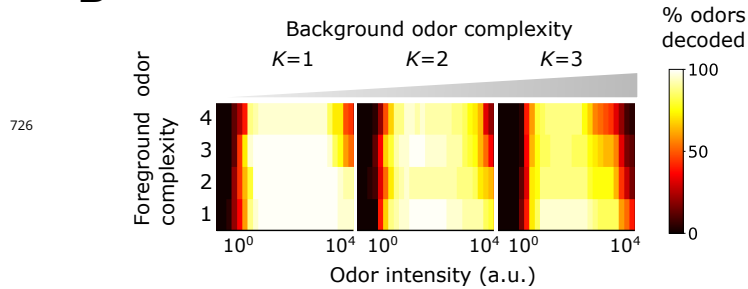
A**B**

Figure 3-Figure supplement 2. Benefits conferred by Weber-Fechner adaptation remain for a broader distribution of baseline adapted activity levels A_{0a} , now assumed to be ORN-dependent and chosen from a normal distribution. **A** Distribution of A_{0a} . **B** Decoding accuracy of foreground odors in the presence of background odors.

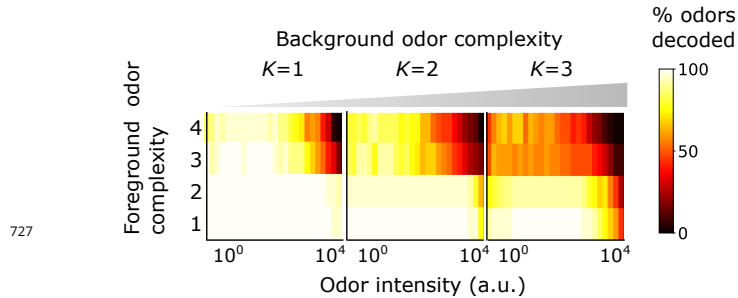


Figure 3-Figure supplement 3. Benefits conferred by Weber-Fechner adaptation remain for 2 binding sites per receptor. This might conceivably occur in insect olfactory receptors, heterotramers consisting of 4 Orco/Or subunits that gate a central ion channel pathway (*Butterwick et al., 2018*). Plotted is the decoding accuracy of foreground odors in the presence of background odors.

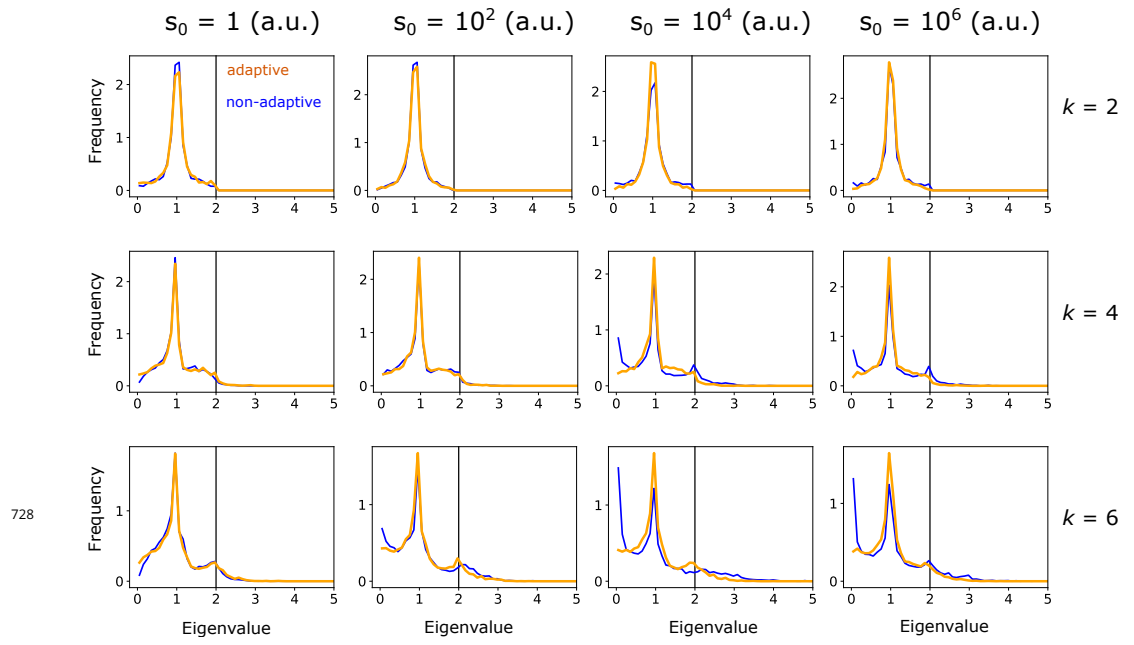


Figure 3–Figure supplement 4. Eigenvalue distribution of $\mathbf{D}_s^T \mathbf{D}_s$, where \mathbf{D}_s is a $m \times k$ submatrix of the column-normalized linearized ORN response matrix \mathbf{D} , evaluated at the linearization point s . Note that s is k -sparse, but its components do not necessarily align with the k columns chosen for the sub-matrix. Eigenvalues are calculated for the adaptive (orange) and non-adaptive (blue) systems, for 1000 randomly chosen linearization points s and submatrices. Plots are arranged for various odor sparsities (by row) and odor intensities (by column). The restricted isometry property is satisfied when the eigenvalues lie between 0 and 2 (black vertical line), and is more strongly satisfied the more centered the distribution is around unity. The increase in near-zero eigenvalues for the non-adaptive system at higher odor complexities and intensities (lower right plots) indicates the weaker fulfillment of the restricted isometry property for these signals, and leads to higher probability of failure in compressed sensing signal reconstruction.

728

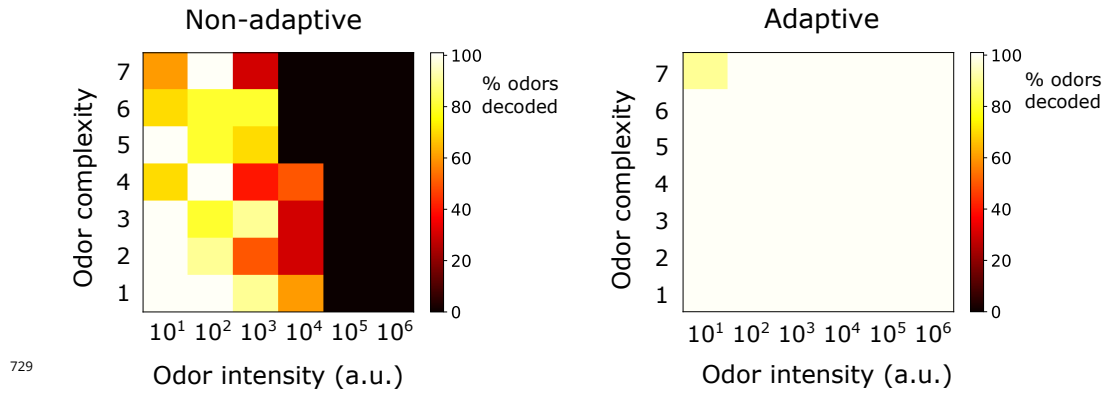


Figure 3-Figure supplement 5. Decoding of odor signals (no background odors) using the IHT algorithm (*Blumensath and Davies, 2009b; Blumensath, 2013*) qualitatively reproduces the results from the main text, which used traditional CS with background linearization. In the adaptive case, IHT actually exhibits superior accuracy to traditional CS, though IHT demands more compute time. The results here show odor decoding accuracy for sparse odor signals of given complexity and intensity, averaged over 10 distinct identities. The iterative algorithm was initialized at $\hat{s} = \mathbf{0}$ and run forward until \hat{s} was stationary, or 10000 iterations were reached. Step size μ in Eq. 25 was set to $s_0/20$. At each step, the linearized response used in determining \mathbf{x}_{i+1} (\mathbf{D}_{s_i} in Eq. 25) was evaluated at the result of i th iteration, \mathbf{x}_i . IHT also requires an assumption on the number of components in the mixture (which defines $H_K(\cdot)$ in Eq. 25); here, that was set to twice the actual sparsity of true signal.

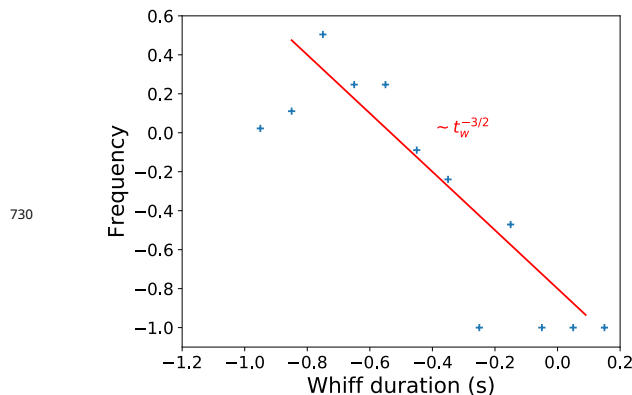


Figure 3-Figure supplement 6. Distribution of whiff durations in naturalistic stimulus, compared to the theoretical prediction (*Celani et al., 2014*)

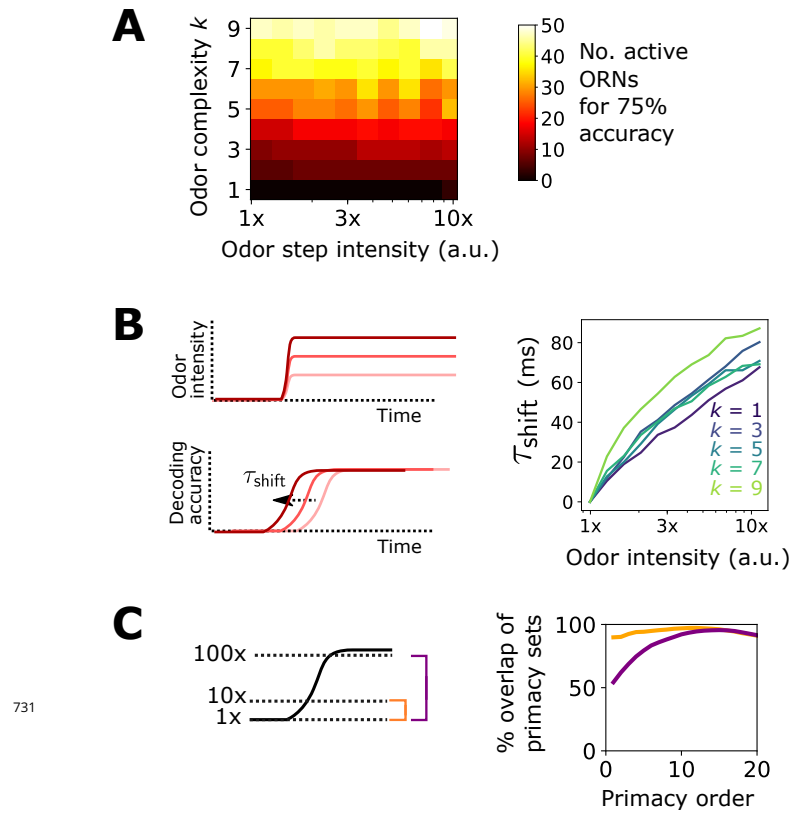


Figure 4-Figure supplement 1. Additional results pertaining to the primacy coding hypothesis. **A** Percent of active ORNs required for 75% accuracy of a steep sigmoidal odor step, as a function of odor step intensity and odor complexity. For low complexities, a primacy set of fewer ORNs may be sufficient to decode the full odor signal; for higher complexities, the entire ORN repertoire is required. **B** In the primacy coding hypothesis, the primacy set is realized sooner for stronger odor signals, so odors are decoded earlier in time, resulting in a perceptual time shift with increasing odor concentration (Wilson et al., 2017). We also find this shift in our compressed sensing decoding framework (right plot), which rises monotonically with step height for various odor complexities, in agreement with primacy coding. **C** The consistency of a primacy code across changes in background odor concentration, in a system with Weber Law adaptation. We calculate the primacy set for odor A (step odor; black) in the presence of either a weak, medium, or strong background (dotted lines; 1x, 10x, 100x a.u.), assuming the system has adapted its response to the background as described in the main text. Averaged across odor A identities, primacy sets for odor A when in the 1x background are nearly identical to those when odor A is in the 10x background (right plot; yellow). The same holds true when comparing the 1x and 100x backgrounds, for sufficiently large primacy order, above 8 or so right plot; purple). This indicates that Weber Law adaptation preserves primacy codes across disparate environmental conditions.

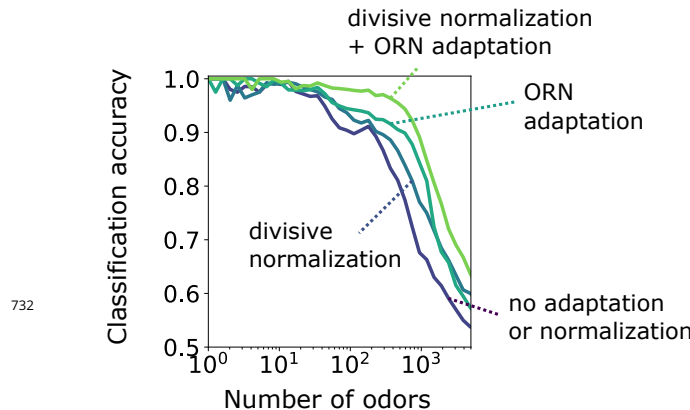


Figure 5–Figure supplement 1. Accuracy of binary classification by odor valence, for odors whose concentrations span a narrow range of concentrations (1 order of magnitude). Accuracy is plotted as a function of the number of distinct odor identities classified by the trained network, in systems with only ORN adaptation, only divisive normalization, both or neither. Decoding gains conferred by divisive normalization and/or ORN adaptation are much smaller than when odors span a much larger range of concentrations, as shown in the main text.